ARCHIVES OF MECHANICS
Arch. Mech. **78** (3), 219–260, 2026, https://doi.org/10.24423/aom.4888

A coupled mechanical-diffusion model for hydrogen-driven ductility degradation

S. SATOURI*), S. MAHMOOD

Capgemini Engineering, 4 avenue Didier Daurat, 31700 Blagnac, France,
e-mail): soheil.satouri@capgemini.com (corresponding author)*

The permeation of hydrogen atoms into metallic structures leads to a variety of unfavorable mechanisms, which result in a reduction in the material's lifespan and unpredictable mechanical failures. In this context, the objective of this work is to model the nonlinear mechanical response of metallic materials as hydrogen diffuses through them. The present investigation is conducted within a fully coupled, thermodynamically consistent mechanical-diffusion framework that incorporates viscoplasticity and damage, and captures the influence of lattice and trapped hydrogen on the mechanical response. As a case study, the model parameters for Inconel 718 are identified and the results are validated using experimental data from literature. A parametric study is carried out to examine the interaction between hydrogen concentration, loading rate, and mechanical responses, with particular emphasis on the ductility loss under increased hydrogen exposure. The results provide clear insight into how hydrogen diffusion interacts with stress, viscoplasticity, and damage, and they enhance our understanding of how the coupling between hydrogen diffusion and ductile mechanisms leads to ductility degradation in the material.

Key words: hydrogen exposure, thermodynamics, damage, loss of ductility.

1. Introduction

For a century, fossil fuels have been the primary energy source worldwide, valued for their energy density, affordability, and ease of extraction. However, this dependence has come at a significant environmental cost, as fossil fuel combustion is one of the major drivers of escalating carbon emissions, contributing to the climate crisis. Addressing this pressing issue has spurred extensive research into alternative energy sources, with the aim of reducing carbon emissions and mitigating the impacts of global warming. Among these alternatives, hydrogen has emerged as a promising candidate due to its potential as a clean and sustainable energy carrier [1–4]. Despite its advantages, the adoption of hydrogen faces significant challenges, particularly in its storage and transportation, which must be addressed to realise its full potential as a viable energy solution.

The use of hydrogen as a future energy source presents several challenges in terms of its adaptability, storage and equipment distribution. One of the most critical challenges is the interaction of hydrogen with materials, which can lead to premature damage and failure under mechanical loading. This phenomenon impacts the safe use of hydrogen across the entire supply chain, including storage, transportation, and consumption, in a wide range of industries. For example, steel pipelines used to transport hydrogen in various forms, metal storage tanks employed in the energy sector, superalloy mechanical components in jet engines within the aerospace industry are all critical applications when hydrogen interactions with materials must be carefully considered. An understanding of the processes and mechanisms of hydrogen embrittlement into the relevant materials can thus help with generating more precise estimates for maintenance intervals to improve material durability. To this end, it is therefore crucial to develop a model predicting the mechanical response and damage coupled with hydrogen diffusion.

The phenomenon of hydrogen penetration and concentration in solids can be split into two phases: diffusion and accumulation. First, small hydrogen atoms penetrate and diffuse into the material through the crystal lattice occupying defects, such as micro-voids, voids, dislocations. Subsequently, the accumulation of hydrogen atoms leads to hydrogen embrittlement and ultimately crack formation. Numerous studies in literature investigate the influence of hydrogen exposure and diffusion in metals, such as reductions in toughness and ductility [5–7]. There are two primary theories that explain the mechanisms leading to degradation of material properties: Hydrogen Enhanced Decohesion (HEDE) and Hydrogen Enhanced Localised Plasticity (HELP). The HEDE mechanism involves atomic hydrogen within the metal lattice, reducing the cohesive energies of the metal bonds leading to hydrogen embrittlement [8]. In this regard, Li and Zhang [9] presented a numerical fracture phase-filed model incorporating the HEDE mechanism and compared the numerical results with experimental data. They defined a hydrogen concentration-dependent fracture parameter connected to a damage variable. In the HELP mechanism, atomic hydrogen facilitates dislocation mechanisms and subsequent damage. In this context, Sofronis and Aravas presented a theoretical model, demonstrating how hydrogen contributes to softening and localisation of plastic flow and bifurcation in numerical models [10]. They assumed that the initial yield strength depends on hydrogen concentration, affecting plastic flow. However, hydrogen embrittlement is often a result of a combination of these mechanisms.

To model material behaviour and damage evolution under hydrogen diffusion, a proper thermodynamic framework is needed. In this context, a suitable free energy function accounting for the chemical potential induced by hydrogen diffusion and concentration must be defined. Podstrigach *et al.* [11, 12],

proposed the first thermodynamic framework to model stress-diffusion coupling which was extended by CAHN and LARCHÉ [13]. In this regard, VILLANI *et al.* [14] developed a thermodynamic basis to model elasto-viscoplastic mechanical responses coupled with hydrogen diffusion. However, their model did not account for a damage variable. Furthermore, ANAND [15] introduced a mechanical-diffusional theory for large elasto-plastic deformations but did not take into account hydrogen diffusion into the trapping sites and its interaction with plasticity. SOFRONIS and MCMEEKING [16] proposed a model linking elastoplastic deformation, nonlinear diffusion and hydrogen trapping, which was later extended to incorporate the lattice-dilatation and the effect of the plastic deformation on trapping sites [17]. Several numerical models based on this framework have since been developed and reported in the literature [18–20].

Although significant progress has been made in modelling hydrogen diffusion and hydrogen-assisted degradation, some limitations still exist. CHARLES *et al.* [19] investigated the effect of transient trapping on hydrogen transport near a blunting crack tip, with particular emphasis on the redistribution of lattice and trapped hydrogen concentrations. However, their study mainly focused on hydrogen transport and trapping kinetics and did not include a complete viscoplastic damage constitutive framework. DEPRAETERE *et al.* [20] proposed a fully coupled continuum damage model for plasticity dominated hydrogen embrittlement mechanisms. Nevertheless, their damage description is based on a Complete Gurson Model (CGM), in which degradation is represented through the evolution of the void volume fraction. Although this approach is well suited for porous ductile fracture, the hydrogen effect is not introduced through a thermodynamic framework coupling hydrogen diffusion mechanisms, viscoplastic flow and ductile damage.

The present work develops a thermodynamically consistent framework for hydrogen-assisted ductility degradation. The proposed formulation integrates lattice and trapped hydrogen transport, hydrogen-induced strain, nonlinear viscoplasticity, and plasticity-driven ductile damage within a unified coupled mechanical-diffusion model. The model is calibrated and validated using experimental stress–strain data for Inconel 718. It is then applied to 0D material-point simulations and 3D finite element analyses under uniaxial loading. This allows the effects of hydrogen concentration, loading rate, stress, and mechanical boundary conditions on plastic deformation and ductile damage evolution to be analyzed consistently.

This paper is organized as follows. Section 2 presents the hydrogen diffusion and the associated mechanisms. Section 3 introduces the thermodynamically consistent framework and derives the constitutive laws. In Section 4, the governing Euler–Lagrange equations are established. Section 5 describes the numerical methodology and its implementation within a finite element framework.

In Section 6, the model parameters are identified using experimental data for Inconel 718, and the model is subsequently validated. Section 7 presents a 0D parametric study to investigate the model response at a material point. Finally, Section 8 examines a 3D geometry subjected to uniaxial loading and discusses the corresponding results.

In this study, a specialized notation style is used to distinguish scalars, vectors and tensors. To this end, lower-case symbols in bold represent vectors, upper-case symbols in bold indicate second-order tensors, upper-case symbols in black represent fourth-order tensors, and other symbols are considered scalars. In terms of tensor and vector products, the following notations are used:

$$\begin{aligned} \boldsymbol{A} : \boldsymbol{B} &= A_{ij}B_{ij}, \quad (\mathbb{A} : \boldsymbol{B})_{ij} = A_{ijkl}B_{kl}, \\ (\boldsymbol{A} \otimes \boldsymbol{B})_{ijkl} &= A_{ij}B_{kl}, \quad \boldsymbol{a} \cdot \boldsymbol{b} = a_i b_i. \end{aligned} \tag{1.1}$$

2. Hydrogen concentration

The impact of hydrogen on the evolution of damage in metals can be identified by measuring variations in hydrogen concentration within the material. Hydrogen atoms can become concentrated in the material through two primary mechanisms: (i) Occupying Normal Interstitial Lattice Sites (NILS) as a result of microstructural features, often referred to as interstitial jumps (C^{L}) and (ii) through trapping at defect sites, such as dislocations, grain boundaries, voids, etc. (C^{T}) [20].

The quantities of C^{L} and C^{T} are respectively the hydrogen concentration in the lattice and the hydrogen concentration in the trap sites, and are defined as follows [16, 20]:

$$C^{\mathrm{L}} = \theta^{\mathrm{L}}\beta^{\mathrm{H}}N^{\mathrm{L}}, \quad C^{\mathrm{T}} = \theta^{\mathrm{T}}\alpha^{\mathrm{H}}N^{\mathrm{T}}, \tag{2.1}$$

where N^{L} and N^{T} denote the densities of lattice sites and trapping sites, respectively. The quantities θ^{L} and θ^{T} are the dimensionless fractional occupancies of lattice and trap sites, respectively, ranging from 0 to 1. They represent the ratio between the number of occupied sites and the total number of sites. With this in mind, the total hydrogen concentration, C^{H}, is expressed as follows:

$$\begin{aligned} C^{\mathrm{H}} &= C^{\mathrm{L}} + C^{\mathrm{T}} \text{ H atom/mm}^3, \quad \text{and} \\ c^{\mathrm{H}} &= c^{\mathrm{L}} + c^{\mathrm{T}} = \frac{c^{\mathrm{L}}}{N^{\mathrm{L}}} + \frac{c^{\mathrm{T}}}{N^{\mathrm{L}}}, \quad \text{H atom/metal atom (H/M)}, \end{aligned} \tag{2.2}$$

where c^{H}, c^{L}, and c^{T} the dimensionless total, lattice, and trapped hydrogen concentrations, respectively, expressed in hydrogen atoms per metal atom.

For further details, refer to SOFRONIS and MCMEEKING [16]; α^{H} and β^{H} values vary depending on the properties of the microstructure. For example, for a tetrahedral configuration of cubic ferrite, we can assume that β^{H} is equal to 6 and if we consider that one trap site corresponds to one interstitial, $\alpha^{\mathrm{H}} = 1$. For austenitic configuration, β^{H} is assumed to be 3, with $\alpha^{\mathrm{H}} = 1$. The lattice metal density, N^{L}, is calculated as follows [20]:

$$N^{\mathrm{L}} = \frac{N^{\mathrm{A}}}{V^{\mathrm{M}}}, \tag{2.3}$$

where N^{A} represents Avogadro's constant equal to 6.022×10^{23} mol^{-1}. Here, V^{M} is the molar volume. Dealing with the trapping mechanism, however, presents greater challenges. The density of trapping sites depends on microstructural defects. The concentration of hydrogen atoms trapped depends on the binding energy of the trap. Hydrogen concentration and diffusion may be either reversible or irreversible. Traps with binding energies above certain values are considered irreversible, and the hydrogen atoms that are trapped inside can no longer escape. Experimental methods such as electrochemical permeation and thermal desorption spectroscopy (TDS) provide valuable insights into trap binding energy and trapping sites [21, 22].

ORIANI [23] implied that there is always an equilibrium between the hydrogen trapped inside the lattice and reversible traps. Following Oriani's theory, reversible traps are assumed to be in thermodynamic equilibrium with interstitial lattice sites. This condition is expressed by the equality of the corresponding chemical potentials:

$$\mu^{\mathrm{L}} = \mu^{\mathrm{T}}. \tag{2.4}$$

For ideal configurational mixing, the chemical potentials can be written as:

$$\begin{aligned} \mu^{\mathrm{L}} &= \mu_L^0 + R^{\mathrm{g}} T \ln\left(\frac{\theta^{\mathrm{L}}}{1-\theta^{\mathrm{L}}}\right), \\ \mu^{\mathrm{T}} &= \mu_T^0 + R^{\mathrm{g}} T \ln\left(\frac{\theta^{\mathrm{T}}}{1-T}\right). \end{aligned} \tag{2.5}$$

Accordingly, Oriani's theory (Eq. (2.4)) can be expressed as follows:

$$\frac{\theta^{\mathrm{T}}}{1-\theta^{\mathrm{T}}} = \frac{\theta^{\mathrm{L}}}{1-\theta^{\mathrm{L}}} \exp\left(\frac{\Delta H^{\mathrm{B}}}{R^{\mathrm{g}} T}\right), \tag{2.6}$$

where R^{g} is the gas constant equal to 8.3144 J $\cdot$ mol^{-1} $\cdot$ K^{-1}, and T represents the absolute temperature. ΔH^{B} represents the trap's binding energy, which is an important parameter for predicting hydrogen diffusion in the material and

is related to the trap's ability to hold hydrogen atoms. The binding energy can be obtained through experimental methods, such as thermal desorption spectroscopy (TDS) [24]. A high binding energy, greater than 60–70 $\mathrm{kJ \cdot mol^{-1}}$, leads to irreversible traps, which are considered not to be part of the diffusion mechanism. In the case of a low NILS concentration:

$$\theta^{\mathrm{L}} \ll 1. \tag{2.7}$$

Considering Eq. (2.6) and Eq. (2.1), the following equation is derived:

$$C^{\mathrm{T}} = \frac{\frac{C^{\mathrm{L}}\alpha^{\mathrm{H}}N^{\mathrm{T}}}{\beta^{\mathrm{H}}N^{\mathrm{L}}}\exp\left(\frac{\Delta \mathrm{H}^{\mathrm{B}}}{R^{\mathrm{g}}T}\right)}{1+\frac{C^{\mathrm{L}}}{\beta^{\mathrm{H}}N^{\mathrm{L}}}\exp\left(\frac{\Delta \mathrm{H}^{\mathrm{B}}}{R^{\mathrm{g}}T}\right)}. \tag{2.8}$$

Equation (2.8) can be presented also with respect to c^{L} and c^{T}:

$$c^{\mathrm{T}} = \frac{\frac{c^{\mathrm{L}}\alpha^{\mathrm{H}}N^{\mathrm{T}}}{\beta^{\mathrm{H}}N^{\mathrm{L}}}\exp\left(\frac{\Delta \mathrm{H}^{\mathrm{B}}}{R^{\mathrm{g}}T}\right)}{1+\frac{c^{\mathrm{L}}}{\beta^{\mathrm{H}}}\exp\left(\frac{\Delta \mathrm{H}^{\mathrm{B}}}{R^{\mathrm{g}}T}\right)}. \tag{2.9}$$

The density of trapping sites, N^{T}, originates from microstructural defects, such as grain boundaries and dislocations. For microstructural defects, the densities of trapping sites are often considered constant. However, the sites corresponding to dislocation defects vary under loading and subsequent plastic deformation. In this context, KUMNICK and JOHNSON [7] carried out an experimental study and explored hydrogen trapping in deformed iron. Their observations enabled them to express the density of trapped dislocations, N^{T} , as a function of accumulated plastic strain, p, as follows [16]:

$$\log N^{\mathrm{T}} = 23.26 - 2.33\exp(-5.5p). \tag{2.10}$$

This allows us to examine how C^{T} varies as a function of C^{L} using the current model. Considering $V^{\mathrm{M}} = 6.5 \times 10^{-6}$ $\mathrm{m^3/mol}$, $\beta^{\mathrm{H}} = 3$, $\alpha^{\mathrm{H}} = 1$, and $T = 298\,^{\circ}\mathrm{K}$, the variation of trapped hydrogen concentration relative to lattice hydrogen is illustrated in Eq. (2.8) shows a 3D representation of the interaction between C^{T}, C^{L} and p. As observed, at higher values of equivalent plastic strain, the trapped hydrogen concentration increases with greater inclination relative to the lattice hydrogen concentration. In the following sections, the constitutive laws are formulated using dimensionless hydrogen concentrations, c^{H}, c^{L}, and c^{T}. This normalization expresses the hydrogen content relative to the density of lattice sites, providing a physically meaningful measure of hydrogen occupancy and simplifying the coupling terms in the constitutive laws.

3. Constitutive laws and thermodynamic background

In order to characterise the thermodynamic behaviour of the material, state variables are introduced to describe its condition. Two types of state variables are considered: observable and internal state variables. Observable variables such as strain, $\boldsymbol{\epsilon}$, are measurable, while internal state variables represent unmeasurable quantities that capture the internal mechanisms of the materials.

In this context, strain, $\boldsymbol{\epsilon}$, is taken as the observable state variable. The material exhibits dissipative and irreversible mechanisms, which depend on the internal state variables. The total strain is expressed as:

$$\boldsymbol{\epsilon} = \boldsymbol{\epsilon}^{\mathrm{e}} + \boldsymbol{\epsilon}^{\mathrm{vp}} + \boldsymbol{\epsilon}^{\mathrm{h}}, \tag{3.1}$$

where $\boldsymbol{\epsilon}^{\mathrm{e}}$, $\boldsymbol{\epsilon}^{\mathrm{vp}}$, and $\boldsymbol{\epsilon}^{\mathrm{h}}$ are the elastic, viscoplastic, and hydrogen-induced strains, respectively. Hydrogen induced strain, $\boldsymbol{\epsilon}^{\mathrm{h}}$, is introduced to account for the local volumetric deformation due to hydrogen insertion and the associated lattice relaxation. It should be noted that this strain must not be interpreted as resulting directly from the physical volume of interstitial hydrogen atoms. The volumetric effect of hydrogen may also be affected by point defects, particularly hydrogen stabilized vacancies and hydrogen vacancy complexes [25, 26]. Atomistic studies show that hydrogen strongly interacts with vacancies in BCC iron and promote the stability of H-vacancy clusters [27]. More recent DFT results have confirmed the role of point defects and tensorial stress effects on hydrogen diffusion in BCC iron [28]. Since the present framework does not include vacancy concentration, vacancy transport, or hydrogen vacancy complex evolution as additional internal variables, this effect is represented phenomenologically through an effective relaxation volume, represented as hydrogen induced strain [29]:

$$\boldsymbol{\epsilon}^{\mathrm{h}} = \frac{V^{\mathrm{H}}}{3V^{\mathrm{M}}}(c^{\mathrm{L}} - c^{\mathrm{L}}_{\mathrm{ref}})\boldsymbol{I}, \tag{3.2}$$

where c^{L} is the dimensionless lattice hydrogen concentration, $c^{\mathrm{L}}_{\mathrm{ref}}$ is the reference dimensionless lattice hydrogen concentration, V^{M} is the molar volume of the host metal, and V^{H} is an effective relaxation volume. This parameter should be understood as a chemical expansion coefficient accounting for local lattice relaxation. A more detailed description of vacancy assisted swelling would require additional internal variables describing vacancy density and hydrogen vacancy complex formation, which is beyond the scope of the present study.

When the material is subjected to a hydrogen flux, its behaviour is modelled using a thermodynamic potential (Ψ). This potential accounts for elasto-viscoplastic deformation, ductile damage, and hydrogen diffusion. Considering

the hydrogen exposure, the thermodynamic potential is divided into two components: the chemical potential (Ψ^{chm}) and the mechanical potential (Ψ^{mec}), as described in [14, 30, 31]

$$\Psi = \Psi^{\mathrm{mec}} + \Psi^{\mathrm{chm}}, \tag{3.3}$$

with:

$$\begin{aligned}\rho\Psi^{\mathrm{mec}} &= \frac{1}{2}(1-D)\boldsymbol{\epsilon}^{\mathrm{e}} : \mathbb{C}^{\mathrm{e}} : \boldsymbol{\epsilon}^{\mathrm{e}} \\ &\quad + R^{\infty}\left[p + \frac{1}{b}(\exp(-bp) - 1\right)] + \frac{\eta}{3}\boldsymbol{\xi} : \boldsymbol{\xi},\end{aligned} \tag{3.4}$$

$$\rho\Psi^{\mathrm{chm}} = \frac{E^{\mathrm{f}}c^{\mathrm{L}}}{V^{\mathrm{M}}} + \frac{R^{\mathrm{g}}T}{V^{\mathrm{M}}}(c^{\mathrm{L}}\ln(c^{\mathrm{L}}) + (1-c^{\mathrm{L}})\ln(1-c^{\mathrm{L}})). \tag{3.5}$$

Here, D denotes the damage, which is treated as a scalar internal state variable. $\mathbb{C}^{\mathrm{e}}$ denotes the fourth order stiffness tensor. R^{∞} and b are scalar hardening parameters, and $\boldsymbol{\xi}$ is the back strain internal state variable.

The state laws can be derived as:

$$\begin{aligned}&\boldsymbol{\sigma} = \rho\frac{\partial\Psi}{\partial\boldsymbol{\epsilon}}, \quad -Y = \rho\frac{\partial\Psi}{\partial D}, \quad -\boldsymbol{\sigma} = \rho\frac{\partial\Psi}{\partial\boldsymbol{\epsilon}^{\mathrm{vp}}}, \quad R = \rho\frac{\partial\Psi}{\partial p}, \\ &\mu = \rho\frac{\partial\Psi}{\partial c^{\mathrm{L}}}, \qquad \boldsymbol{\chi} = \rho\frac{\partial\Psi}{\partial\boldsymbol{\xi}},\end{aligned} \tag{3.6}$$

where $\boldsymbol{\chi}$ denotes the back stress tensor, and μ represents the conjugate state variable (diffusion potential) of the hydrogen concentration. The expression for μ is derived as:

$$\begin{aligned}\mu &= \rho\frac{\partial\Psi}{\partial c^{\mathrm{L}}} \\ &= \frac{\partial\boldsymbol{\epsilon}}{\partial c^{\mathrm{L}}} : \boldsymbol{\sigma} + \frac{R^{\mathrm{g}}T}{V^{\mathrm{M}}}[\ln(c^{\mathrm{L}}) - \ln(c^{\mathrm{L}}-1)] + \frac{E^{\mathrm{f}}}{V^{\mathrm{M}}} \\ &= -\frac{V^{\mathrm{H}}}{3V^{\mathrm{M}}}\mathrm{tr}(\boldsymbol{\sigma}) + \frac{R^{\mathrm{g}}T}{V^{\mathrm{M}}}\left[\ln\left(\frac{c^{\mathrm{L}}}{c^{\mathrm{L}}-1}\right) + \frac{E^{\mathrm{f}}}{R^{\mathrm{g}}T}\right] \\ &= -\frac{V^{\mathrm{H}}}{V^{\mathrm{M}}}\sigma^{\mathrm{hyd}} + \frac{R^{\mathrm{g}}T}{V^{\mathrm{M}}}\left[\ln\left(\frac{c^{\mathrm{L}}}{c^{\mathrm{L}}-1}\right) + \frac{E^{\mathrm{f}}}{R^{\mathrm{g}}T}\right].\end{aligned} \tag{3.7}$$

The thermodynamic framework is described using state variables and their conjugates, as derived in the state laws given in Eq. (3.6). State variables, including the observable strain ($\boldsymbol{\epsilon}$) and internal state variables ($D, \boldsymbol{\epsilon}^{\mathrm{vp}}, p, c^{\mathrm{L}}$, and $\boldsymbol{\xi}$), are summarised in Table 1.

TABLE 1. State and conjugate state variables.

State variable		Conjugate state variable
Observable	Internal	
$\boldsymbol{\epsilon}$	–	$\boldsymbol{\sigma}$
–	D	$-Y$
–	$\boldsymbol{\epsilon}^{\mathrm{vp}}$	$-\boldsymbol{\sigma}$
–	p	R
–	c^{L}	μ
–	$\boldsymbol{\xi}$	$\boldsymbol{\chi}$

Replacing the Helmholtz free energy into the global Clausius–Duhem inequality (derived in detail in Appendix A) yields:

$$
\begin{aligned}
&\mathcal{D} = \boldsymbol{\sigma} : \dot{\boldsymbol{\epsilon}} - \rho\dot{\Psi} - \boldsymbol{\nabla}\cdot(\mu\boldsymbol{j}) \geq 0,\\
&\mathcal{D} = \boldsymbol{\sigma} : \dot{\boldsymbol{\epsilon}} - \rho\left(\frac{\partial\Psi}{\partial\boldsymbol{\epsilon}} : \dot{\boldsymbol{\epsilon}} + \frac{\partial\Psi}{\partial\boldsymbol{\epsilon}^{\mathrm{vp}}} : \dot{\boldsymbol{\epsilon}}^{\mathrm{vp}} + \frac{\partial\Psi}{\partial D}\dot{D} + \frac{\partial\Psi}{\partial p}\dot{p} + \frac{\partial\Psi}{\partial\boldsymbol{\xi}} : \dot{\xi} + \frac{\partial\Psi}{\partial c^{\mathrm{L}}}\dot{c}^{\mathrm{L}}\right)\\
&\qquad - \boldsymbol{\nabla}\cdot(\mu\boldsymbol{j}) \geq 0\\
&\qquad = \boldsymbol{\sigma} : \dot{\boldsymbol{\epsilon}} - \boldsymbol{\sigma} : \dot{\boldsymbol{\epsilon}} + \boldsymbol{\sigma} : \dot{\boldsymbol{\epsilon}}^{\mathrm{vp}} + Y\dot{D} - R\dot{p} - \boldsymbol{\chi} : \dot{\boldsymbol{\xi}} - \mu\dot{c}^{\mathrm{L}} - \boldsymbol{\nabla}\cdot(\mu\boldsymbol{j}) \geq 0\\
&\qquad = \boldsymbol{\sigma} : \dot{\boldsymbol{\epsilon}}^{\mathrm{vp}} + Y\dot{D} - R\dot{p} - \boldsymbol{\chi} : \dot{\boldsymbol{\xi}} - \mu\dot{C}^{\mathrm{L}} - \boldsymbol{\nabla}\cdot(\mu\boldsymbol{j}) \geq 0\\
&\qquad = \boldsymbol{\sigma} : \dot{\boldsymbol{\epsilon}}^{\mathrm{vp}} + Y\dot{D} - R\dot{p} - \boldsymbol{\chi} : \dot{\boldsymbol{\xi}} - \mu\dot{C}^{\mathrm{L}} - \boldsymbol{j}\boldsymbol{\nabla}\mu - \mu\boldsymbol{\nabla}\cdot(\boldsymbol{J}) \geq 0,\\
&\mathcal{D} = \boldsymbol{\sigma} : \dot{\boldsymbol{\epsilon}}^{\mathrm{vp}} + Y\dot{D} - R\dot{p} - \boldsymbol{\chi} : \dot{\boldsymbol{\xi}} - \boldsymbol{j}\cdot\boldsymbol{\nabla}\mu \geq 0.
\end{aligned}
\tag{3.8}
$$

The above inequality represents the simplified Clausius–Duhem inequality, encapsulating both the first and second laws of thermodynamics within the framework of the present model. The evolution laws are derived from specific convex dual potentials: a mechanical dual potential for viscoplasticity, hardening and damage, and a chemical/diffusion dual potential for hydrogen transport. To capture the Bauschinger effect (i.e., asymmetrical behaviour of metals), a nonlinear kinematic hardening model is employed [32]. It should be noted that the kinematic hardening contribution is included to provide a more general constitutive framework capable of representing the Bauschinger effect. However, the present study focuses on monotonic tensile loading, and the Bauschinger effect is not specifically investigated or calibrated in this work. To this end, non-associative plasticity is used, and the normality laws are derived using the following convex indicator functions:

$$
F^{\mathrm{mec}} = f + f^{\chi} + f^{\mathrm{D}},
\tag{3.9}
$$

with:

$$
\begin{aligned}
f &= \frac{\mathrm{eq}(\boldsymbol{\sigma}-\boldsymbol{\chi})}{1-D} - R - R^{\mathrm{o}}, \qquad f^{\chi} = \frac{3\gamma}{4\eta}\boldsymbol{\chi}:\boldsymbol{\chi}, \\
f^{\mathrm{D}} &= \frac{S^{\mathrm{D}}}{(\beta^{\mathrm{D}}+1)(1-D)}\left(\frac{Y}{S}\right)^{\beta^{\mathrm{D}}+1},
\end{aligned}
\tag{3.10}
$$

where γ is the hardening-related material parameter. S^{D} and β^{D} are the damage-related parameters. R is the isotropic hardening function defined as [33, 34]:

$$
R = R^{\infty}[1-\exp(-bp)], \tag{3.11}
$$

where R^{∞} is the hardening-related parameter. By maximising dissipation and applying Kuhn–Tucker conditions, the evolution laws corresponding to plasticity and damage are derived as follows:

$$
\begin{aligned}
&\dot{p} = \dot{\lambda}, \qquad \dot{\boldsymbol{\epsilon}}^{\mathrm{vp}} = \frac{\partial F^{\mathrm{mec}}}{\partial \boldsymbol{\sigma}}\dot{\lambda} = \boldsymbol{\Lambda}^{\mathrm{vp}}\dot{\lambda}, \qquad \dot{D} = \frac{\partial F^{\mathrm{mec}}}{\partial Y}\dot{\lambda} = \Lambda^{\mathrm{D}}\dot{\lambda}, \\
&\dot{\boldsymbol{\xi}} = -\frac{\partial F^{\mathrm{mec}}}{\partial \boldsymbol{\chi}}\dot{\lambda} = \boldsymbol{\Lambda}^{\mathrm{bs}}\dot{\lambda},
\end{aligned}
\tag{3.12}
$$

where λ is the Lagrange multiplier, and $\boldsymbol{\Lambda}^{\mathrm{vp}}$, Λ^{D}, and $\boldsymbol{\Lambda}^{\mathrm{bs}}$ are the viscoplastic, the damage, and the back strain flows, respectively, and are obtained as:

$$
\boldsymbol{\Lambda}^{\mathrm{vp}} = \frac{3}{2}\frac{\boldsymbol{\sigma}' - \boldsymbol{X}'}{\mathrm{eq}(\boldsymbol{\sigma}-\boldsymbol{X})}, \quad \Lambda^{\mathrm{D}} = \frac{1}{(1-D)}\left(\frac{Y}{S^{\mathrm{D}}}\right)^{\beta^{\mathrm{D}}}, \quad \boldsymbol{\Lambda}^{\mathrm{bs}} = \boldsymbol{\Lambda}^{\mathrm{vp}} - \frac{3\gamma}{2\eta}\boldsymbol{\chi}. \tag{3.13}
$$

To incorporate the viscoplastic response, the evolution of λ is linked to the yield function via the following relation:

$$
\dot{\lambda} = \left(\frac{\langle f\rangle_{+}}{R^{\mathrm{vp}}}\right)^{P^{\mathrm{vp}}}, \tag{3.14}
$$

where R^{vp} and P^{vp} are the viscoplasticity parameters. For the chemical component, a convex dual potential is expressed as follows [14]:

$$
\phi^{\mathrm{chm}} = \frac{1}{2}\boldsymbol{L}(c^{\mathrm{L}}) : \boldsymbol{\nabla}\mu \otimes \boldsymbol{\nabla}\mu, \tag{3.15}
$$

where $\boldsymbol{L}(c^{\mathrm{L}})$ denotes the hydrogen mobility tensor. The details of deriving the evolution laws are provided in Appendix A. Considering the evolution laws, the hydrogen flux is obtained as:

$$
\boldsymbol{j} = -\frac{\partial \phi^{\mathrm{chm}}}{\partial \boldsymbol{\nabla}\mu}. \tag{3.16}
$$

Considering isotropic diffusion, the hydrogen mobility is expressed as:

$$\boldsymbol{L}(c^{\mathrm{L}}) = L(c^{\mathrm{L}})\boldsymbol{I} = \frac{D^{\mathrm{H}}V^{\mathrm{M}}}{R^{\mathrm{g}}T}c^{\mathrm{L}}\left(1-c^{\mathrm{L}}\right)\boldsymbol{I}. \tag{3.17}$$

Using Eq. (3.7), the gradient of chemical potential is derived as:

$$\begin{aligned}\boldsymbol{\nabla}\mu &= \frac{R^{\mathrm{g}}T}{V^{\mathrm{M}}}(\boldsymbol{\nabla}\ln(c^{\mathrm{L}}) - \boldsymbol{\nabla}\ln(c^{\mathrm{L}}-1)) + \frac{V^{\mathrm{H}}}{V^{\mathrm{M}}}\boldsymbol{\nabla}\sigma^{\mathrm{hyd}} \\ &= \frac{R^{\mathrm{g}}T}{V^{\mathrm{M}}}\left[\left(\frac{1}{c^{\mathrm{H}}}\right)\frac{\nabla c^{\mathrm{L}}}{c^{\mathrm{L}}-1}\right] + \frac{V^{\mathrm{H}}}{V^{\mathrm{M}}}\boldsymbol{\nabla}\sigma^{\mathrm{hyd}}.\end{aligned} \tag{3.18}$$

Replacing Eq. (3.15) and Eq. (3.17) into Eq. (3.16) yields:

$$\begin{aligned}\boldsymbol{j} &= -\frac{\partial\left(\frac{1}{2}\frac{D^{\mathrm{H}}V^{M}}{R^{\mathrm{g}}T}c^{\mathrm{L}}(1-c^{\mathrm{L}})\boldsymbol{I}:\boldsymbol{\nabla}\mu\otimes\boldsymbol{\nabla}\mu\right)}{\partial\boldsymbol{\nabla}\mu} \\ &= -\frac{D^{\mathrm{H}}V^{M}}{R^{\mathrm{g}}T}c^{\mathrm{L}}(1-c^{\mathrm{L}})\boldsymbol{\nabla}\mu.\end{aligned} \tag{3.19}$$

Replacing the Eq. (3.18) into the Eq. (3.19), the hydrogen flux, $\boldsymbol{j}$, is derived as:

$$\boldsymbol{j} = -D^{\mathrm{H}}\left[\boldsymbol{\nabla}c^{\mathrm{L}} - \frac{c^{\mathrm{L}}V^{\mathrm{H}}}{R^{\mathrm{g}}T}\boldsymbol{\nabla}\sigma^{\mathrm{hyd}}\right]. \tag{3.20}$$

The constitutive laws, derived in this section, are briefly listed in Table 2, which are implemented on the numerical model in the following sections. A detailed presentation of the formulation and the corresponding derivations is provided in Appendix A.

TABLE 2. Constitutive laws of the elastoplastic model accounted for ductile damage and hydrogen exposure. Here, $\boldsymbol{\Lambda}^{\mathrm{vp}} = \frac{3}{2}\frac{\boldsymbol{\sigma}'}{\boldsymbol{\sigma}^{\mathrm{eq}}}$ and $\boldsymbol{\Lambda}^{\mathrm{D}} = \left(\frac{\mathbf{Y}}{\mathbf{S}^{\mathrm{D}}}\right)^{\boldsymbol{\beta}^{\mathrm{D}}}$, $\boldsymbol{\Lambda}^{\mathrm{bs}} = \boldsymbol{\Lambda}^{\mathrm{vp}} - \frac{3\gamma}{2\boldsymbol{\eta}}\boldsymbol{\chi}$, and $\boldsymbol{\Lambda}^{\mathrm{H}} = \boldsymbol{\nabla}\boldsymbol{c}^{\mathrm{L}} + \frac{\boldsymbol{C}^{\mathrm{L}}\boldsymbol{V}^{\mathrm{H}}}{R^{g}T}\boldsymbol{\nabla}\boldsymbol{\sigma}^{\mathrm{hyd}}$.

State variables	Conjugate state variable	Evolution laws
Observable:		
$\boldsymbol{\epsilon}$	$\boldsymbol{\sigma} = \rho\frac{\partial\Psi}{\partial\boldsymbol{\epsilon}}$	–
Internal:		
$\boldsymbol{\epsilon}^{\mathrm{vp}}$	$-\boldsymbol{\sigma} = \rho\frac{\partial\Psi}{\partial\boldsymbol{\epsilon}^{\mathrm{vp}}}$	$\dot{\boldsymbol{\epsilon}}^{\mathrm{vp}} = \frac{\partial F^{\mathrm{mec}}}{\partial\boldsymbol{\sigma}}\dot{\lambda} = \boldsymbol{\Lambda}^{\mathrm{vp}}\dot{\lambda}$
$\boldsymbol{\xi}$	$\boldsymbol{\chi} = \rho\frac{\partial\Psi}{\partial\boldsymbol{\xi}}$	$\dot{\boldsymbol{\xi}} = \frac{\partial F^{\mathrm{mec}}}{\partial\boldsymbol{\chi}}\dot{\lambda} = \boldsymbol{\Lambda}^{\mathrm{bs}}\dot{\lambda}$
p	$R = \rho\frac{\partial\Psi}{\partial p}$	$\dot{p} = \dot{\lambda}$
D	$-Y = \rho\frac{\partial\Psi}{\partial D}$	$\dot{D} = \frac{\partial F^{\mathrm{mec}}}{\partial Y}\dot{\lambda} = \Lambda^{\mathrm{D}}\dot{\lambda}$
c^{L}	$\mu = \rho\frac{\partial\Psi}{\partial c^{\mathrm{L}}}$	–
–	–	$\boldsymbol{j} = -\frac{\partial\phi^{\mathrm{chm}}}{\partial\boldsymbol{\nabla}\mu} = -D^{\mathrm{H}}\boldsymbol{\Lambda}^{\mathrm{H}}$

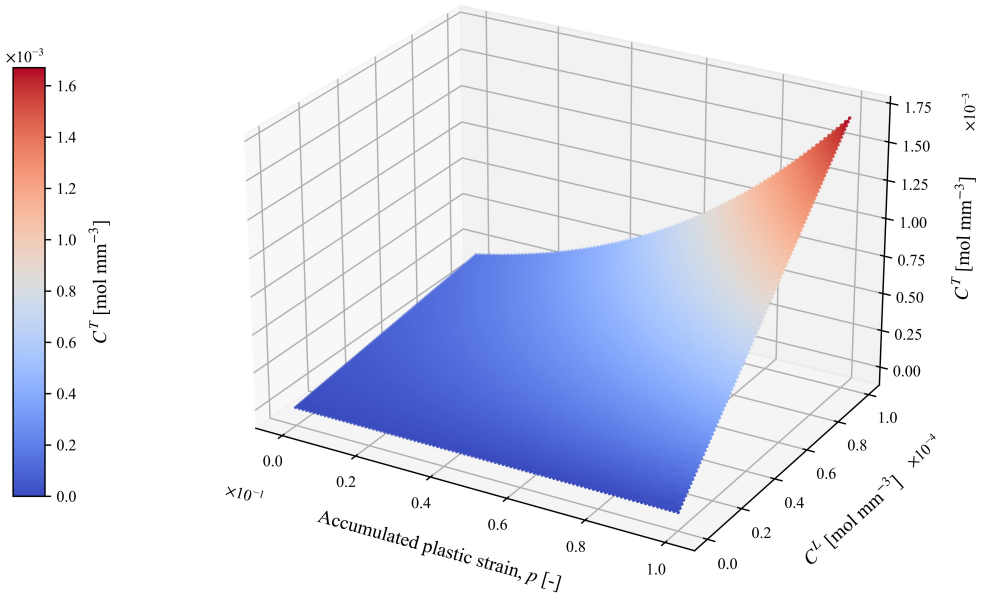

FIG. 1. Variation of trapped hydrogen concentration versus lattice hydrogen concentration, and plastic deformation.

4. Euler–Lagrange equations

The governing equations are written in weak form. The mechanical weak form follows from the classical principle of virtual work:

$$\int_{\Omega} \boldsymbol{\sigma} : \boldsymbol{\nabla}\delta\boldsymbol{u}\,\mathrm{d}V - \int_{\Omega} \boldsymbol{f}^{\mathrm{b}} \cdot \delta\boldsymbol{u}\,\mathrm{d}V - \int_{\partial\Omega} \boldsymbol{f}^{\mathrm{s}} \cdot \delta\boldsymbol{u}\,\mathrm{d}S = 0. \tag{4.1}$$

The diffusion weak form is obtained from the hydrogen mass conservation equation using a weighted-residual formulation:

$$\int_{\Omega} \left(\frac{\partial c^{\mathrm{H}}}{\partial t}\delta\mu - \boldsymbol{j} \cdot \boldsymbol{\nabla}\delta\mu \right) \mathrm{d}V + \int_{\partial\Omega} q^{\mathrm{o}}\delta\mu\,\mathrm{d}S = 0, \tag{4.2}$$

where $\delta\boldsymbol{u}$ is the virtual displacement field, $\delta\mu$ is the scalar test function associated with the chemical potential field, and q^{o} denotes the hydrogen flux on the boundary. Using the divergence theorem, Eq. (4.1) and Eq. (4.2) are reformulated as:

$$(4.3)\quad -\int_{\Omega}\boldsymbol{\nabla}\cdot\boldsymbol{\sigma}\cdot\delta\boldsymbol{u}\,\mathrm{d}V+\int_{\partial\Omega}\boldsymbol{\sigma}\cdot\boldsymbol{n}\cdot\delta\boldsymbol{u}\,\mathrm{d}S-\int_{\Omega}\boldsymbol{f}^{\mathrm{b}}\cdot\delta\boldsymbol{u}\,\mathrm{d}V-\int_{\partial\Omega}\boldsymbol{f}^{\mathrm{s}}\cdot\delta\boldsymbol{u}\,\mathrm{d}S=0,$$
$$\int_{\Omega}\left(\frac{\partial c^{\mathrm{H}}}{\partial t}+\boldsymbol{\nabla}\cdot\boldsymbol{j}\right)\delta\mu\,\mathrm{d}V+\int_{\partial\Omega}\boldsymbol{j}\cdot\boldsymbol{n}\delta\mu\,\mathrm{d}S-\int_{\partial\Omega}q^{\mathrm{o}}\delta\mu\,\mathrm{d}S=0.$$

Accordingly, the corresponding governing equations and boundary conditions are obtained as:

$$(4.4)\qquad \boldsymbol{\nabla}\cdot\boldsymbol{\sigma}+\boldsymbol{f}^{\mathrm{b}}=\boldsymbol{0}\ \forall\boldsymbol{x}\in\Omega\ \text{with}\ \boldsymbol{\sigma}\cdot\boldsymbol{n}-\boldsymbol{f}^{\mathrm{s}}=\boldsymbol{0}\ \forall\boldsymbol{x}\in\partial\Omega,$$

$$(4.5)\qquad \boldsymbol{\nabla}\cdot\boldsymbol{j}+\frac{\partial c^{\mathrm{H}}}{\partial t}=0\ \forall\boldsymbol{x}\in\Omega\ \text{with}\ \boldsymbol{j}\cdot\boldsymbol{n}-q^{\mathrm{o}}=0\ \forall\boldsymbol{x}\in\partial\Omega,$$

where Eq. (4.5) represents the mass conservation equation, and the hydrogen flux, $\boldsymbol{j}$, can be replaced using the flux-related evolution law, Eq. (3.20) [14, 17]:

$$(4.6)\qquad \frac{\partial c^{\mathrm{H}}}{\partial t}+\boldsymbol{\nabla}\cdot\left[-D^{\mathrm{H}}\left(\boldsymbol{\nabla}c^{\mathrm{L}}+\frac{c^{\mathrm{L}}V^{\mathrm{H}}}{RT}\boldsymbol{\nabla}\sigma^{\mathrm{hyd}}\right)\right]=0.$$

Considering the hydrogen concentration equilibrium between trapped and NILS sites, Eq. (2.9) is substituted into the Eq. (4.6):

$$(4.7)\qquad \left[\frac{c^{\mathrm{L}}+c^{\mathrm{T}}(1-\theta^{\mathrm{T}})}{c^{\mathrm{L}}}\right]\frac{\partial c^{\mathrm{L}}}{\partial t}$$
$$=-\boldsymbol{\nabla}\cdot\left[-D^{\mathrm{H}}\left(\boldsymbol{\nabla}c^{\mathrm{L}}+\frac{c^{\mathrm{L}}V^{\mathrm{H}}}{RT}\boldsymbol{\nabla}\sigma^{\mathrm{hyd}}\right)\right]-\theta^{\mathrm{T}}\alpha^{\mathrm{H}}\frac{\partial N^{\mathrm{T}}}{\partial p}\frac{\partial p}{\partial t}.$$

5. Numerical implementation

Mass transfer and stress equilibrium equations, along with their associated boundary conditions constitute a non-linear set of equations. This system is solved through a finite element computational model. To that end, an implicit Euler backward scheme is applied to discretise the constitutive equations in time. To update the internal state variables, an iterative process, known as the "convex cutting plane", is employed, which is divided into two steps: i) elastic prediction and ii) viscoplastic correction/prediction (see Appendix B).

For the elastic prediction, it is assumed that only the elastic mechanism is active, with no damage or plasticity occurring ($\delta\boldsymbol{\epsilon}^{\mathrm{vp}}=\boldsymbol{0}$, $\delta p=\delta D=0$). As long as the yield function remains zero or negative, the mechanical responses stay in the elastic zone ($f\leq 0$), and the elastic prediction remains valid. Once the equivalent stress exceeds the elastic limit, R^{o}, the yield function becomes positive ($f>0$), and the viscoplastic flow is activated. In the second step,

viscoplastic correction/prediction, all internal variables are taken into account, and the nullity of the following criterion must be satisfied:

$$\phi^{\mathrm{vp}} = \dot{p} - \left(\frac{\langle f \rangle_+}{R^{\mathrm{vp}}}\right)^{P^{\mathrm{vp}}} = 0. \tag{5.1}$$

All discretized equations and the numerical procedure are explained in detail in Appendix B. In the following section, the model parameters are identified using experimental data from literature using a home-made 0D solver (for a single point).

6. Parameters identification and model validation

As previously mentioned, the model can be applied to a wide range of metals. Here, as a case study, Inconel (nickel-based superalloy) is considered to perform a parametric study on the mechanical response and damage of metallic structures in hydrogen-rich environments. To this end, the 0D home-made solver is developed to identify the model parameters and validate the results using experimental data given by MORETTI *et al.* [35]. The material chemical composition is listed in Table 3.

TABLE 3. INCONEL chemical composition [35].

Element	Ni	Fe	Cr	Nb	Mo	Ti	Al
Wt. Pct	49.62±1.35	17.58±0.49	17.18±0.49	4.75 ±0.20	2.58±0.12	1.08±0.06	0.43±0.05

Due to the limited experimental database, the identified parameters should not be interpreted as a unique material parameter set. The kinematic hardening parameters cannot be independently identified from monotonic tensile tests alone because stress reversal or cyclic tests would be required. The present parameter set is therefore used as a representative reference response for the subsequent coupled mechanical-diffusion sensitivity analyses. Considering the nonlinear viscoplastic behaviour, experimental data from monotonic tests conducted at two different loading rates 1 s^{-1} and 0.001 s^{-1} are utilised for model calibration. To this end, the Nelder–Mead optimisation method is employed. The Nelder–Mead method is a heuristic optimisation approach aimed at minimising the cost function by comparing and sorting function values, without the need for derivatives. Further details can be found in [36, 37]. The calibration results are plotted and illustrated in Fig. 2. As observed, the model responses closely match the experimental data, demonstrating good agreement. The identified parameters are provided and listed in Table 4.

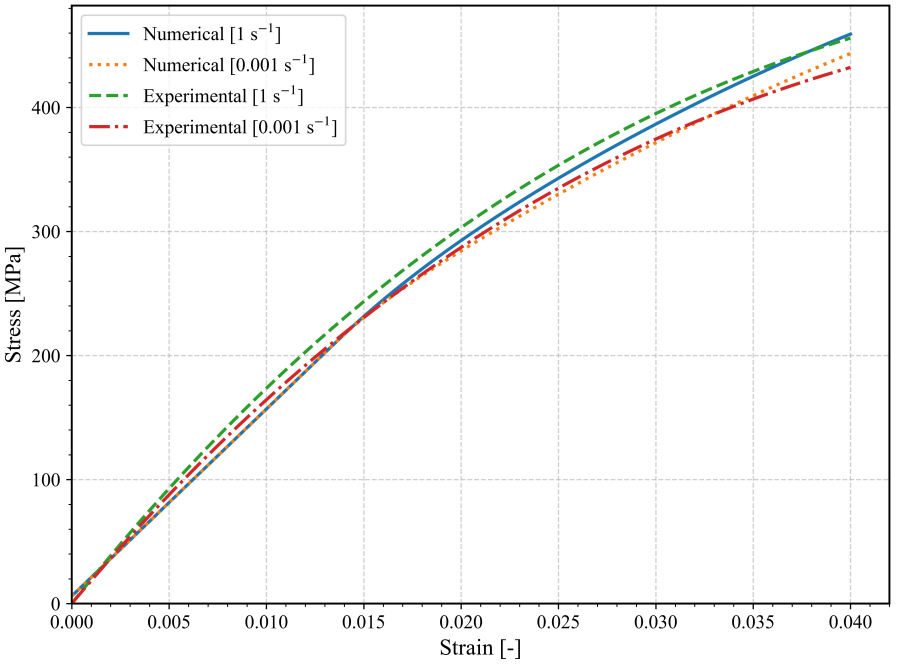

FIG. 2. Stress-strain curves at 1 s^{-1} and 0.001 s^{-1} and comparison with the experimental data.

Using the identified parameters given in Table 4, the model mechanical response is validated against the experimental data at the loading rate of 0.01 s^{-1}. As observed, the numerical results show good agreement with the experimental

TABLE 4. Model parameters identified for INCONEL 718.

Mechanism	Model parameter [unit]	Value
Elasticity	ν [–]	0.30
	E [MPa]	1.12×10^4
Viscoplasticity	R^{o} [MPa]	122.48
	P^{vp} [–]	1.09
	R^{vp} [MPa$^{1/P^{\mathrm{vp}}}$]	24.10
	b [–]	29.81
	R^{∞}	124.00
	η [MPa]	8.55×10^5
	γ [–]	398.92
Damage	β^{D} [–]	0.29
	S^{D} [MPa]	6.3×10^{-3}

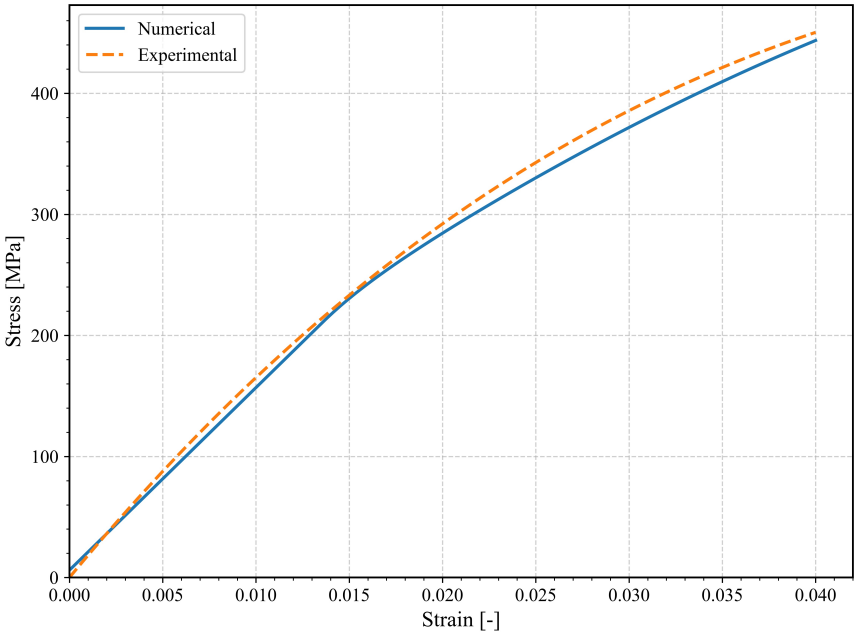

Fig. 3. Validation of numerical results with experimental data with 0.01 s^{-1} loading rate.

data. It should be noted that the current calibration process does not guarantee a unique and independent identification of all parameters associated with the different mechanisms in the model. Additional experimental data, including loading-unloading paths, different hydrogen concentrations, and local measurements of hydrogen distribution would be required to capture all mechanisms. Therefore, the identified parameter set is used here as a physically consistent reference calibration, sufficient to establish the baseline mechanical response and to support the subsequent parametric analyses of hydrogen-assisted ductility degradation.

7. 0D model sensitivity analysis

This section investigates, at the materialpoint level, how hydrogen affects the viscoplastic response and ductile damage in the proposed coupled framework. To this end, a parametric study based on the coupled mechanical-diffusion model is conducted using a 0D solver developed as a python script through the standard libraries. A monotonic strain-controlled load along the X-axis, with a strain rate of 5×10^{-4} s^{-1}, is applied to the considered single point. Material properties are assumed to be those of an austenitic nickel-base superalloy, as listed in Table 4. The hydrogen diffusion model parameters are also provided in Table 5.

TABLE 5. Hydrogen diffusion parameters for Nickel-based superalloy Inconel 718.

Model parameter [unit]	Value
$c_{\mathrm{ref}}^{\mathrm{L}}$ [H/M]	1×10^{-30}
D^{H} [$\mathrm{mm}^2\cdot\mathrm{s}^{-1}$]	5.3×10^{-7}
α^{H} [–]	1
β^{H} [–]	3
ΔH^{B} [$\mathrm{J}\cdot\mathrm{mol}^{-1}$]	30×10^{3}
R^{g} [$\mathrm{J}\cdot\mathrm{mol}^{-1}\cdot\mathrm{K}^{-1}$]	8.314
V^{M} [$\mathrm{mm}^3\cdot\mathrm{mol}^{-1}$]	6.77×10^{3}
V^{H} [$\mathrm{mm}^3\cdot\mathrm{mol}^{-1}$]	2×10^{3}

The evolution of the accumulated plastic strain with respect to time at different lattice hydrogen concentration is plotted in Fig. 4. For all cases, the material response remains elastic during the initial loading stage, and plastic deformation initiates after approximately $t = 30$ s. After the onset of plasticity, p increases with respect to time. However, its magnitude decreases as the lattice hydrogen concentration increases. This indicates that, within the present constitutive framework, hydrogen reduces the amount of accumulated

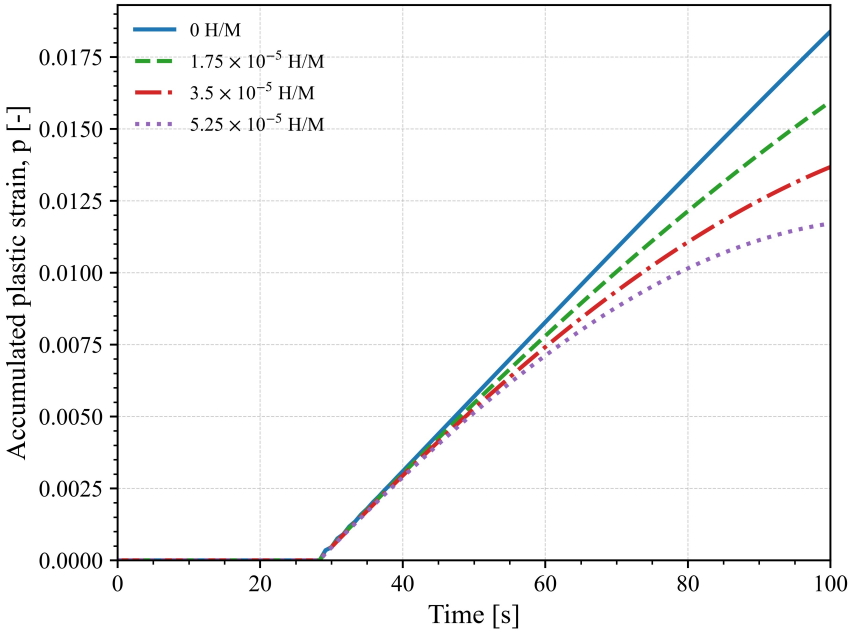

FIG. 4. Evolution of accumulated plastic strain with respect to time at different hydrogen concentration.

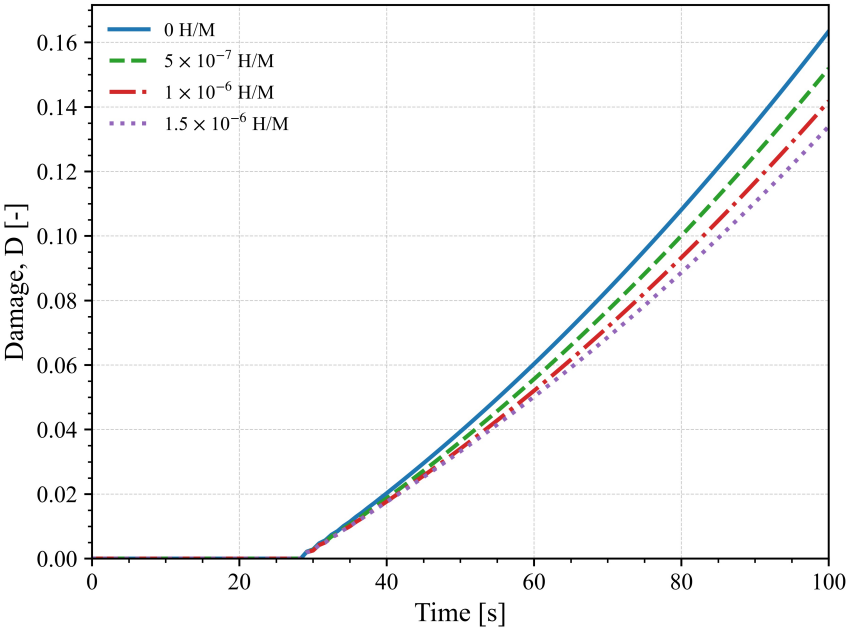

FIG. 5. Evolution of damage with respect to time at different hydrogen concentration.

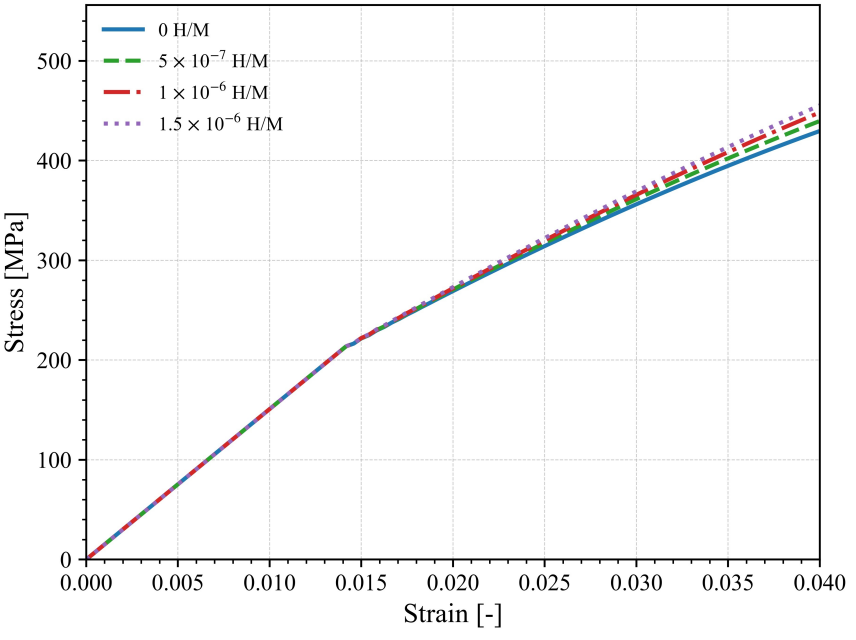

FIG. 6. Stress-strain curves at different hydrogen concentration with the strain rate of 5×10^{-4} s^{-1}.

viscoplastic deformation under the same loading level. Since the ductile damage evolution is driven by accumulated viscoplastic strain through the evolution laws given by Eq. (3.12), the reduction of p also decreases the subsequent ductile damage evolution (Fig. 5). In the present framework, embrittlement is expressed through the loss of ductility, and a more brittle-like mechanical response. This interpretation is supported by the stress-strain curves shown in Fig. 6. The stress-strain response is plotted at different hydrogen concentrations under monotonic strain-controlled loading. As observed, increasing hydrogen concentration increases the yield stress and the overall stress level, indicating a reduced tendency for plastic flow and a more brittle-like mechanical response. However, the material may still be more prone to brittle failure under hydrogen diffusion, which would require the incorporation of an additional brittle damage mechanism in future extensions of the model.

In the next section, the developed framework is implemented in a finite element model to provide a better understanding of hydrogen embrittlement in 3D structures and its influence on viscoplastic deformation and ductile damage.

8. 3D model sensitivity analysis

In this section, the notched plate is considered as a 3D geometry for the parametric study under uniaxial loading conditions. The corresponding dimensions, loading and boundary conditions are shown in Fig. 7. The model parameters and physical properties are given in Table 4 and Table 5. For the finite element computation, an 8-node linear brick element is employed to mesh the given structure in all analyses. The simulations are performed using a finite element model developed for this study. The discretization scheme, element formulation, and solution strategy are described in detail in Appendix C.

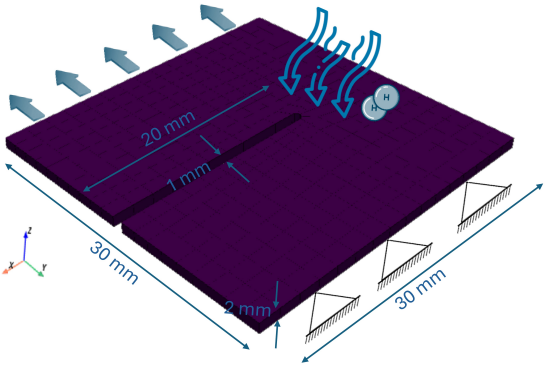

FIG. 7. Dimensions, loading, and boundary conditions of the notched plate.

A uniform, monotonic displacement-controlled load of 0.3 mm along the y-axis is applied to the structure, as shown in Fig. 7, while the displacement components are set to zero on the opposite side. The initial lattice hydrogen concentration, $c^{\mathrm{L}}_{\mathrm{ref}}$, is assumed to be uniform in the specimen. Hydrogen ingress is implemented by applying the constant Neumann flux, q^{o} on all external surfaces, as given in Eq. (4.5), with the sign chosen considering the outward normal convention. No Dirichlet condition on the lattice hydrogen concentration is imposed. The hydrogen flux is maintained at 1×10^{-15} mm $\cdot$ s^{-1}. The analysis is carried out for different loading rates: i) 1×10^{-3} mm$\cdot$s^{-1}, ii) 5×10^{-4} mm$\cdot$s^{-1}, and iii) 2.5×10^{-4} mm $\cdot$ s^{-1}. The distribution of ductile damage, accumulated plastic strain, and trapped hydrogen concentration are provided in Fig. 8. The three fields are mainly localized in the vicinity of the notch. The localization is not perfectly symmetric because one side of the specimen is clamped, while the opposite side is subjected to the displacement-controlled loading. The mechanical fields are influenced by the global boundary conditions, and the plasticity driven damage extends from the notch toward the mechanically active zone. The intensity of the trapped hydrogen concentration field is affected by the loading rate. At lower loading rates, the longer exposure time allows more hydrogen diffusion and trapping, leading to a higher trapped hydrogen concentration. It is also observed that the accumulated plastic strain and the ductile damage intensity are more pronounced at lower loading rates. In the present model, at a lower loading rate, the material has more time to develop viscoplastic deformation

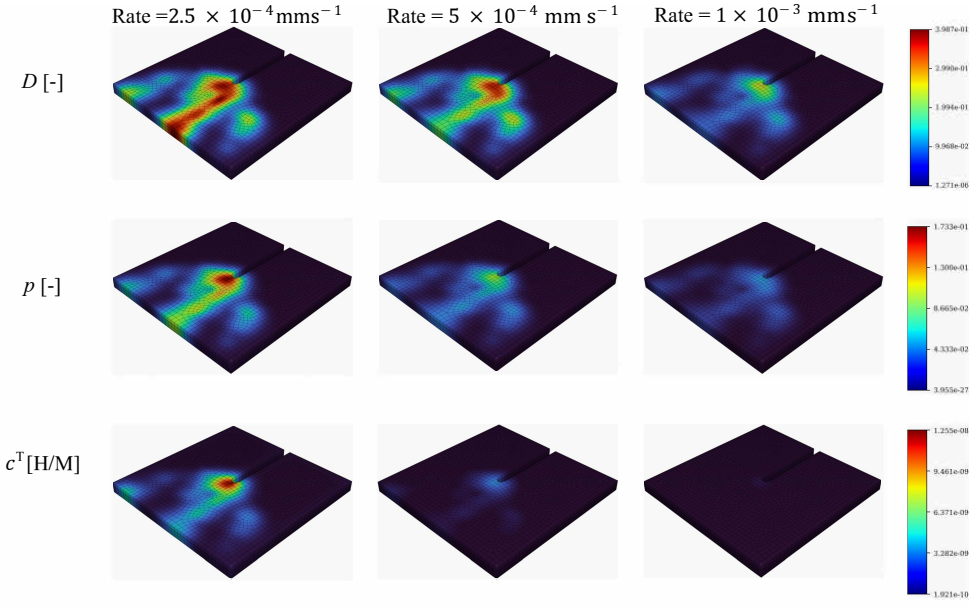

FIG. 8. Hydrogen concentration and damage at different uniaxial loading rates.

during the loading process. Therefore, for the same final displacement, the accumulated plastic strain and consequently ductile damage increases. It should also be noted that the damage variable considered as the ductile damage driven by accumulated viscoplastic deformation. Therefore, its distribution follows the plastic strain field rather than a brittle crack-tip fracture process. The trapped hydrogen concentration exhibits a similar tendency because the density of trapping sites is also governed by the accumulated plastic strain. Hence, regions with higher plastic deformation promote higher trapped hydrogen concentration.

Figure 9 shows the time evolution of the same fields at a fixed loading rate of 2.5×10^{-4}. As time increases, the ductile damage, the accumulated plastic strain, and the trapped hydrogen concentration increase in magnitude while remaining localised around the notch and along the mechanically active zone.

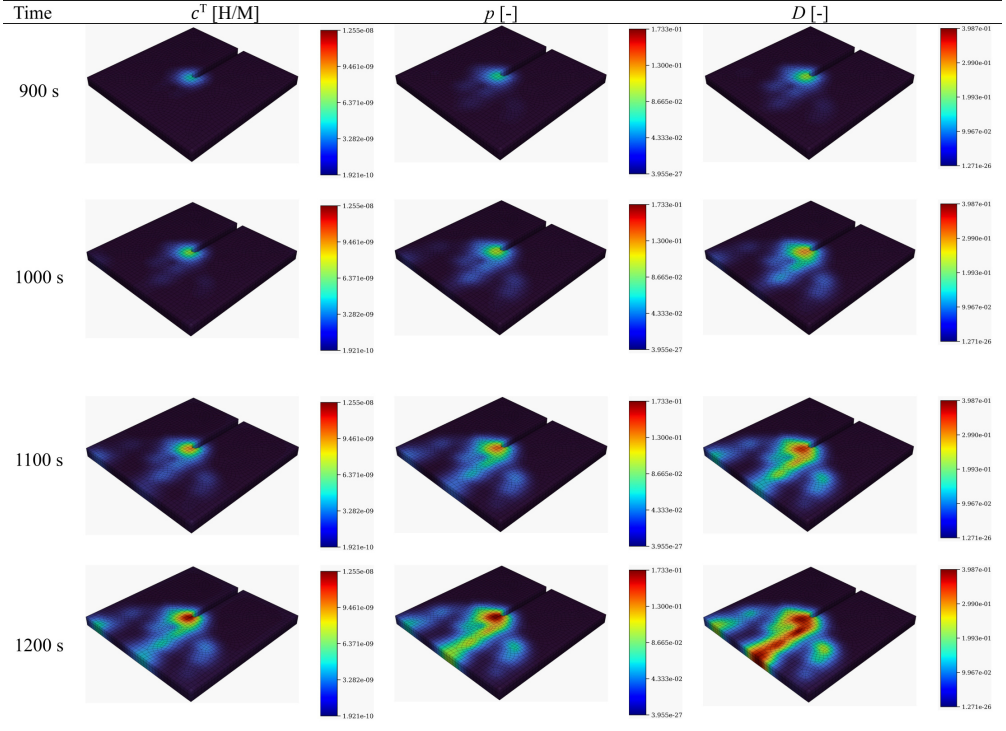

FIG. 9. Hydrogen concentration and damage under 0.3 mm uniaxial displacement-controlled load with a rate of 2.5×10^{-4} mm $\cdot$ s^{-1} over time.

Figure 10 illustrates the temporal evolution of the von Mises stress distribution under a uniaxial displacement-controlled loading condition, with the displacement of 0.225 mm applied at the rate of 2.5×10^{-4} mm $\cdot$ s^{-1}. At $t = 900$ s, the von Mises stress is moderately distributed, with stress concentration mainly developing around the notch region. By $t = 1100$ s, the stress field becomes

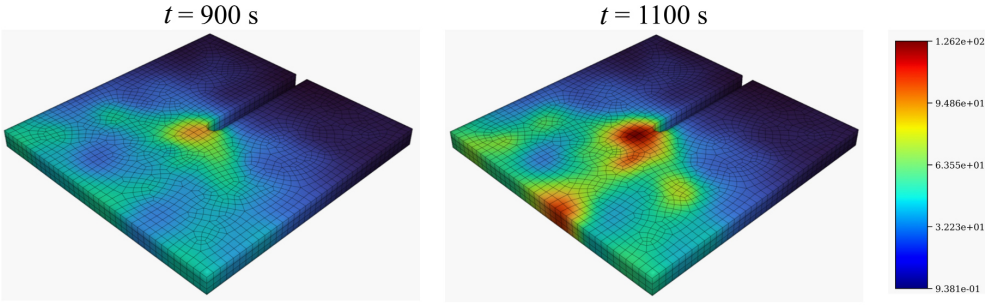

Fig. 10. von Mises stress [MPa] distribution under 0.225 mm uniaxial displacement-controlled load with a rate of 2.5×10^{-4} mm $\cdot$ s^{-1}.

more strongly localized near the notch, with increased peak values and sharper stress gradients. This evolution indicates progressive deformation and stress localization, which is consistent with the development of plastic flow and damage accumulation.

9. Conclusions and perspectives

In this study, a fully coupled mechanical-diffusion model was developed to analyse the mechanical response and ductile damage behaviour of metals exposed to hydrogen. Grounded in thermodynamic principles, the model integrates a thermodynamic potential that combines both mechanical and chemical behaviours, allowing for the derivation of state and evolution laws coupling hydrogen concentration and mechanical responses. The model was calibrated and validated against experimental data for the nickel-based superalloy Inconel 718, showing satisfactory agreement between the numerical predictions and the experimental stress–strain responses. The developed framework provides a comprehensive understanding of the effect of hydrogen concentrations in both lattice and trapped sites on the growth of the ductile damage.

Through parametric analyses 0D and 3D models under uniaxial loading, we highlighted a consistent correlation between trapped hydrogen accumulation and ductile damage and accumulated plasticity, particularly near mechanical stress concentrators where plastic flow also localizes. Moreover, an increase in lattice hydrogen content delays the onset of viscoplasticity and reduces the magnitude of plastic deformation, which subsequently lowers the ductile damage rate because the ductile damage is explicitly plasticity-driven based on the evolution laws. This trend reflects the fact that the current model captures hydrogen-induced ductility loss, while brittle mechanisms associated with hydrogen embrittlement are not included in the present framework and can be incorporated

in future extensions. These results provide a clearer understanding of hydrogen's impact on ductile mechanisms and the resulting loss of ductility.

This study focused on the analysis of ductile damage and its interaction with hydrogen atoms. To obtain a more complete view, a combination of brittle and ductile mechanisms can be taken into account [43, 44]. This extension would provide a better understanding of the balance between ductile and brittle mechanisms under hydrogen exposure. Additionally, performing mechanical tests under hydrogen exposure and studying the ductile and brittle behaviour of the samples could help identify new mechanisms to enhance the reliability of the model. Moreover, the high damage levels and fracturing of metals under mechanical loading in hydrogen-rich environments require applying nonlocal approaches, such as gradient enhancement or phase-field methods [45–47], to capture accurate responses, particularly in finite element computations.

The monotonic loading discussed in this paper can be extended to cyclic loading and fatigue analysis, which would better describe the operating environments for most metal components exposed to hydrogen [48, 49]. Since cyclic analyses using finite element methods can be computationally expensive, the constitutive laws presented could be replaced by a data-driven framework through the non-intrusive Proper Generalised Decomposition (PGD) method [50, 51].

Appendix A. Thermodynamic background

A.1. Dissipation inequality

In this appendix, the equations used in the thermodynamic equations are derived in detail. Since it is necessary to develop the constitutive laws considering thermodynamic constraints, here, dissipation for an elasto-plastic material with hydrogen diffusion coupling is derived based on the Clausius–Duhem inequality. To this end, the first and second laws of thermodynamics are used to derive dissipation as a function of the present mechanisms. The first law of thermodynamics in the rate form is expressed as:

$$P^{\text{ext}} + Q^* = \dot{U} + \dot{K}, \tag{A.1}$$

where P^{ext} is the power coming from external forces. Q^* is the thermal power. $\dot{U}$ and $\dot{K}$ denote the rate of the internal and kinetic energy, respectively. The internal energy in domain Ω is derived as:

$$U = \int_{\Omega} \rho e \, \mathrm{d}V, \tag{A.2}$$

where, in the rate form, it is given by:

$$\dot{U} = \int_{\Omega} \rho \dot{e} \, \mathrm{d}V, \tag{A.3}$$

where e denotes the specific internal energy per unit mass. The kinetic energy is derived as a function of the displacement rate (speed), $\dot{u}$, as:

$$K = \int_{\Omega} \frac{1}{2} \rho \dot{\boldsymbol{u}} \cdot \dot{\boldsymbol{u}} \, \mathrm{d}V, \tag{A.4}$$

where it can be similarly expressed in the rate form as:

$$\dot{K} = \int_{\Omega} \rho \dot{\boldsymbol{u}} \cdot \ddot{\boldsymbol{u}} \, \mathrm{d}V. \tag{A.5}$$

Considering the stress equilibrium, above can be expressed as:

$$\dot{K} = \int_{\Omega} (\boldsymbol{\nabla} \cdot \boldsymbol{\sigma} + \boldsymbol{F_b}) \cdot \dot{\boldsymbol{u}} \, \mathrm{d}V = \int_{\Omega} (\boldsymbol{\nabla} \cdot (\boldsymbol{\sigma} \cdot \dot{\boldsymbol{u}}) - \boldsymbol{\sigma} : \boldsymbol{\nabla} \dot{\boldsymbol{u}} + \boldsymbol{F_b} \cdot \dot{\boldsymbol{u}}) \, \mathrm{d}V. \tag{A.6}$$

Using the divergence theorem and Eq. (A.6), the following is derived:

$$\dot{K} = \int_{\Omega} \boldsymbol{F}_v \cdot \dot{u} + \int_{\partial\Omega} \boldsymbol{F}_s \cdot \dot{\boldsymbol{u}} \, \mathrm{d}S - \int_{\Omega} \boldsymbol{\sigma} : \dot{\boldsymbol{\epsilon}} \, \mathrm{d}V, \tag{A.7}$$

where the first two terms denote the power related to the external body forces and surface tractions, and the third term corresponds to the internal power.

The thermal power is obtained through integration of surface heat flux and internal thermal sources on the domain volume:

$$Q^* = \int_{\partial\Omega} q_s \, \mathrm{d}S + \int_{\Omega} \omega \, \mathrm{d}V, \tag{A.8}$$

where q_{s} denotes surface heat flux, and ω is the internal heat source. The termal power can be also derived as:

$$\int_{\partial\Omega} q_{\mathrm{s}} \, \mathrm{d}S = - \int_{\partial\Omega} \boldsymbol{q} \cdot \boldsymbol{n} \, \mathrm{d}S. \tag{A.9}$$

Using the divergence theorem, the integral on the surface can be reformulated as a volume integral as:

$$\int_{\partial\Omega} \boldsymbol{q} \cdot \boldsymbol{n} \, \mathrm{d}S = \int_{\Omega} \boldsymbol{\nabla} \cdot \boldsymbol{q} \, \mathrm{d}V. \tag{A.10}$$

Accordingly, the total thermal power is derived as:

$$Q^* = -\int_\Omega \boldsymbol{\nabla}\cdot\boldsymbol{q}\,\mathrm{d}V + \int_\Omega \omega\,\mathrm{d}V. \tag{A.11}$$

Getting back to Eq. (A.1) and substituting Eqs. (A.11) and (A.7) yields:

$$-\int_\Omega \boldsymbol{\nabla}\cdot\boldsymbol{q}\,\mathrm{d}V + \int_\Omega \omega\,\mathrm{d}V = -\int_\Omega \boldsymbol{\sigma}:\dot{\boldsymbol{\epsilon}}\,\mathrm{d}V + \int_\Omega \rho\dot{e}\,\mathrm{d}V. \tag{A.12}$$

Finally, the first law of thermodynamics is derived as:

$$\rho\dot{e} = \boldsymbol{\sigma}:\dot{\boldsymbol{\epsilon}} - \boldsymbol{\nabla}\cdot\boldsymbol{q} + \omega. \tag{A.13}$$

The second law of thermodynamics implies that the rate of generated entropy is equal to or greater than the total thermal power divided by the temperature:

$$\frac{\mathrm{d}S}{\mathrm{d}t} \geq \int_{\partial\Omega} \frac{q_s}{T}\,\mathrm{d}S + \int_\Omega \frac{\omega}{T}\,\mathrm{d}V + \int_{\partial\Omega} \frac{\mu\boldsymbol{j}}{T}\cdot\boldsymbol{n}\,\mathrm{d}S. \tag{A.14}$$

The entropy can be defined as follows so that both sides can be returned in the integral form:

$$S = \int_\Omega \rho s\,\mathrm{d}V, \quad \text{and} \quad \dot{S} = \int_\Omega \rho\dot{s}\,\mathrm{d}V. \tag{A.15}$$

Substituting Eq. (A.15) into Eq. (A.14) and using the divergence theorem, Eq. (A.14) is obtained as follows:

$$\int_\Omega \rho\dot{s}\,\mathrm{d}V \geq -\int_\Omega \boldsymbol{\nabla}\cdot\left(\frac{\boldsymbol{q}}{T}\right)\mathrm{d}V + \int_\Omega \frac{\omega}{T}\,\mathrm{d}V + \int_{\partial\Omega} \boldsymbol{\nabla}\cdot\left(\frac{\mu\boldsymbol{j}}{T}\right)\mathrm{d}V. \tag{A.16}$$

Where it can be reduced to the following inequality:

$$\rho\dot{s} \geq -\boldsymbol{\nabla}\cdot\left(\frac{\boldsymbol{q}}{T}\right) + \frac{\omega}{T} + \boldsymbol{\nabla}\cdot\left(\frac{\mu\boldsymbol{J}}{T}\right), \text{ or } \rho\dot{s} + \boldsymbol{\nabla}\cdot\left(\frac{\boldsymbol{q}}{T}\right) - \frac{\omega}{T} - \boldsymbol{\nabla}\cdot\left(\frac{\mu\boldsymbol{j}}{T}\right) \geq 0. \tag{A.17}$$

Substituting the internal source energy related power from Eq. (A.13) into Eq. (A.17) yields:

$$\begin{aligned} &\rho\dot{s} + \boldsymbol{\nabla}\left(\frac{\boldsymbol{q}}{T}\right) - \boldsymbol{\nabla}\cdot\left(\frac{\mu\boldsymbol{j}}{T}\right) - \frac{1}{T}(\rho\dot{e} - \boldsymbol{\sigma}:\dot{\boldsymbol{\epsilon}} + \boldsymbol{\nabla}\cdot\boldsymbol{q}) \\ &= \rho\dot{s}T + \boldsymbol{\nabla}\cdot\boldsymbol{q} - \frac{\boldsymbol{q}\cdot\boldsymbol{\nabla}T}{T} - \boldsymbol{\nabla}\cdot(\mu\boldsymbol{j}) - \frac{\mu\boldsymbol{J}\cdot\boldsymbol{\nabla}T}{T} - \rho\dot{e} + \boldsymbol{\sigma}:\dot{\boldsymbol{\epsilon}} - \boldsymbol{\nabla}\cdot\boldsymbol{q} \\ &= \rho(T\dot{s} - \dot{e}) - \frac{\boldsymbol{q}\cdot\boldsymbol{\nabla}T}{T} - \boldsymbol{\nabla}\cdot(\mu\boldsymbol{j}) - \frac{\mu\boldsymbol{j}\cdot\boldsymbol{\nabla}T}{T} + \boldsymbol{\sigma}:\dot{\boldsymbol{\epsilon}} - \boldsymbol{\nabla}\cdot\boldsymbol{q} \geq 0. \end{aligned} \tag{A.18}$$

In this step, the Helmholtz free energy is introduced as:

$$\Psi = e - Ts. \tag{A.19}$$

Taking the derivative with respect to time, Eq. (A.19), in the rate form, is derived as:

$$\dot{\Psi} = \dot{e} - \dot{T}s - T\dot{s}. \tag{A.20}$$

From Eq. (A.20), the term $T\dot{s}$ is replaced into Eq. (A.18):

$$\begin{aligned} \rho(\dot{e} - \dot{T}s - \dot{\Psi} - \dot{e}) - \frac{\boldsymbol{q}\cdot\boldsymbol{\nabla}T}{T} - \boldsymbol{\nabla}\cdot(\mu\boldsymbol{j}) - \frac{\mu\boldsymbol{j}\cdot\boldsymbol{\nabla}T}{T} + \boldsymbol{\sigma}:\dot{\boldsymbol{\epsilon}} - \boldsymbol{\nabla}\cdot\boldsymbol{q} \\ = \boldsymbol{\sigma}:\dot{\boldsymbol{\epsilon}} - \rho(\dot{T}s + \dot{\Psi}) - \frac{\boldsymbol{q}\cdot\boldsymbol{\nabla}T}{T} - \boldsymbol{\nabla}\cdot(\mu\boldsymbol{j}) - \frac{\mu\boldsymbol{J}\cdot\boldsymbol{\nabla}T}{T} - \boldsymbol{\nabla}\cdot\boldsymbol{q} \geq 0. \end{aligned} \tag{A.21}$$

Equation (A.21) denotes the global dissipation inequality which can be decomposed into two parts:

$$\mathcal{D} = \mathcal{D}^{\mathrm{m}} + \mathcal{D}^{\mathrm{t}} \geq 0. \tag{A.22}$$

Ignoring the temperature gradient and considering an isothermal condition, the thermal dissipation is cancelled out:

$$\mathcal{D} = \boldsymbol{\sigma}:\dot{\boldsymbol{\epsilon}} - \rho\dot{\Psi} - \boldsymbol{\nabla}\cdot(\mu\boldsymbol{J}) \geq 0. \tag{A.23}$$

A.2. Dissipation positivity and pseudo potential

To ensure dissipation positivity, a pseudo-potential, ϕ, is considered as a non-negative convex function that is zero at the reference point. The latter conditions automatically satisfy the positivity of dissipation. This can be simply proved as follows. The differentiable function, ϕ is convex in the $(\boldsymbol{x}_1, \boldsymbol{x}_2)$ if and only if:

$$\phi(\boldsymbol{x}_1) \geq \phi(\boldsymbol{x}_2) + \boldsymbol{\nabla}\phi(\boldsymbol{x}_2)\cdot(\boldsymbol{x}_1 - \boldsymbol{x}_2). \tag{A.24}$$

With this in mind, for $\boldsymbol{x}_1 = \boldsymbol{0}$:

$$\boldsymbol{\nabla}\phi(\boldsymbol{x}_2)\cdot(\boldsymbol{x}_2) \geq \phi(\boldsymbol{x}_2) \geq 0, \tag{A.25}$$

where the term $\boldsymbol{\nabla}\phi(\boldsymbol{x}_2)\cdot(\boldsymbol{x}_2)$ can be expressed as dissipation which is thus non-negative automatically by non-negativity of the pseudo potential, ϕ.

A.3. Dual potential for evolution laws

To ensure that dissipation remains zero or positive, the pseudo-potential, ϕ, is introduced. This pseudo-potential is defined as a non-negative, continuous, and convex scalar function of the state variable fluxes, which equals zero at the reference point:

$$\boldsymbol{\sigma} = \frac{\partial \phi}{\partial \dot{\boldsymbol{\epsilon}}^{\mathrm{vp}}}, \quad Y = \frac{\partial \phi}{\partial \dot{D}}, \quad -R = \frac{\partial \phi}{\partial \dot{p}}, \quad -\boldsymbol{\chi} = \frac{\partial \phi}{\partial \dot{\boldsymbol{\xi}}}, \quad -\boldsymbol{\nabla}\mu = \frac{\partial \phi}{\partial \boldsymbol{j}}. \tag{A.26}$$

The pseudo-potential (ϕ) with the above assumptions, inherently ensures the positivity of dissipation. By applying the Legendre–Fenchel transformation, a dual potential (ϕ^*) is formulated as a function of the conjugate state variables. From this dual potential, the fluxes of the internal state variables can be determined:

$$\begin{aligned} \phi^*(\sigma, X, Y, \boldsymbol{j}) &= [\phi(\dot{\boldsymbol{\epsilon}}^{\mathrm{vp}}, \dot{D}, \dot{p}, \dot{\boldsymbol{\xi}}, \boldsymbol{\nabla}\mu)]^*, \\ \phi^*(\sigma, Y, R, \boldsymbol{\chi}, \boldsymbol{j}) &= \sup_{\dot{\boldsymbol{\epsilon}}^{\mathrm{vp}}, \dot{D}, \dot{p}, \dot{\boldsymbol{\xi}}, \boldsymbol{\nabla}\mu} [\boldsymbol{\sigma} : \dot{\boldsymbol{\epsilon}}^{\mathrm{vp}} + Y\dot{D} - R\dot{p} - \boldsymbol{\chi} : \dot{\boldsymbol{\xi}} - \boldsymbol{j} \cdot \boldsymbol{\nabla}\mu \\ &\qquad - \phi(\dot{\boldsymbol{\epsilon}}^{\mathrm{vp}}, \dot{D}, \dot{p}, \dot{\boldsymbol{\xi}}, \boldsymbol{\nabla}\mu)]. \end{aligned} \tag{A.27}$$

The Legendre–Fenchel transformation yields the convex dual potential (ϕ^*) in an alternative space defined by the conjugate variables. From this dual potential, the evolution laws are derived as:

$$\dot{\boldsymbol{\epsilon}}^{\mathrm{vp}} = \frac{\partial \phi^*}{\partial \boldsymbol{\sigma}}, \quad \dot{D} = \frac{\partial \phi^*}{\partial Y}, \quad -\dot{p} = \frac{\partial \phi^*}{\partial R}, \quad -\dot{\boldsymbol{\xi}} = \frac{\partial \phi^*}{\partial \boldsymbol{\chi}}, \quad -\dot{\boldsymbol{j}} = \frac{\partial \phi^*}{\partial \boldsymbol{\nabla}\mu}. \tag{A.28}$$

A.4. Evolution laws derivation

Plasticity and damage-related evolution laws are derived through dissipation and ensure its positivity. To this end, the Principle of Maximum plasticity Dissipation (PMD) can be used with the yield surface constraints. Here, considering damage introduced by the f^D indicative function, the mechanical indicative function, F^{mec}, is replaced by the yield surface:

$$\lambda F^{\mathrm{mec}} = 0, \quad F^{\mathrm{mec}} \leq 0, \quad \text{and} \quad \lambda \geq 0, \tag{A.29}$$

where λ denotes the Lagrangian multiplier. Considering the above constraints, the Lagrangian equation is expressed as:

$$L^v = Y\dot{D} + \boldsymbol{\sigma} : \dot{\boldsymbol{\epsilon}}^{\mathrm{vp}} - R\dot{p} + \lambda(F^{\mathrm{mec}}). \tag{A.30}$$

To maximize the given Lagrangian with respect to the corresponding conjugate state variables, its gradient is set to zero:

$$\partial_Y L^v = \dot{D} + \lambda \frac{\partial f^D}{\partial Y} = 0, \tag{A.31}$$

$$\partial_{\boldsymbol{\sigma}} L^v = \dot{\boldsymbol{\epsilon}}^{\mathrm{vp}} + \lambda \frac{\partial f}{\partial \boldsymbol{\sigma}} = 0, \tag{A.32}$$

$$\partial_R L^v = -\dot{p} + \lambda \frac{\partial f}{\partial R} = 0, \tag{A.33}$$

where yields the evolution laws as follows:

$$\dot{p} = \lambda \frac{\partial f}{\partial R} = \lambda, \quad \dot{\boldsymbol{\epsilon}}^{\mathrm{vp}} = \lambda \boldsymbol{\Lambda}^{\mathrm{p}}, \quad \dot{D} = -\lambda \Lambda^{\mathrm{D}}. \tag{A.34}$$

For the chemical part of dissipation, a convex dual dissipation potential is introduced as:

$$\phi^{\mathrm{chm}} = \frac{1}{2} \boldsymbol{L}(C^{\mathrm{H}}) : \boldsymbol{\nabla}\mu \otimes \boldsymbol{\nabla}\mu, \tag{A.35}$$

from which, the hydrogen diffusion flux is derived:

$$\dot{\boldsymbol{j}} = \frac{\partial \phi^{\mathrm{chm}}}{\partial \boldsymbol{\nabla}\mu}. \tag{A.36}$$

Appendix B. Numerical implementation

An implicit backward Euler scheme is implemented on the governing equations in order to break down equations to the N time steps, Δt, and each time step, the nullity of viscoplastic criterion has to be satisfied:

$$\phi^{\mathrm{vp}}_{n+1} = \left\langle \frac{f_{n+1}}{R_{vp}} \right\rangle_+^{P_{\mathrm{vp}}^{-1}} - \frac{\Delta p}{\Delta t} \quad \text{with } \Delta p = p_{n+1} - p_n, \tag{B.1}$$

where the von Mises yield function and stress are discretized as:

$$\begin{aligned} f_{n+1} &= f = \frac{\mathrm{eq}(\boldsymbol{\sigma}_{n+1} - \boldsymbol{\chi}_{n+1})}{1 - D} - R_{n+1} - R^{\mathrm{o}}, \\ \boldsymbol{\sigma}_{n+1} &= (1 - D_{n+1}) \mathbb{C}^{\mathrm{e}} : (\boldsymbol{\epsilon}_{n+1} - \boldsymbol{\epsilon}^{\mathrm{vp}}_{n+1}), \\ \boldsymbol{\chi}_{n+1} &= \frac{2c}{3} \boldsymbol{\xi}_{n+1}. \end{aligned} \tag{B.2}$$

B.1. Linearization based on the convex cutting plane

To solve the discretized equation, the convex cutting plane algorithm is used, in which the gradient of flow, $\boldsymbol{\Lambda}^{\mathrm{vp}}$ is ignored. Thus, damage and viscoplastic flow equation variations can be expressed as:

$$\delta\boldsymbol{\epsilon}^{\mathrm{vp}} = \boldsymbol{\Lambda}^{\mathrm{vp}}\delta p, \quad \delta D = \Lambda^{\mathrm{D}}\delta p, \quad \delta\boldsymbol{\xi} = \boldsymbol{\Lambda}^{\mathrm{bs}}\delta p. \tag{B.3}$$

The numerical implementation is divided into two steps: first, elastic prediction, and second viscoplastic correction/prediction. At the first step, it is assumed that the viscoplasticity has not been yet activated. In this case $\delta r = 0$, and consequently $\delta\boldsymbol{\epsilon}^{\mathrm{vp}} = \mathbf{0}$ and $\delta D = 0$, which automatically leads to $\phi^{\mathrm{vp}} = 0$. At the second step, once the von Mises stress exceeds the yield stress, the yield function, f, gets larger than zero, which leads to a positive viscoplastic criterion. In this step, an iterative equation is used to compute δr, through satisfying nullity of the viscoplastic criterion ($\phi^{\mathrm{vp}}= 0$):

$$\phi_{n+1}^{\mathrm{vpi}(k+1)} = \phi_{n+1}^{\mathrm{vp}(k)} + \delta\phi_{n+1}^{\mathrm{vp}(k)}. \tag{B.4}$$

From now on, for more simplicity, k and n indices are ignored. To derive $\delta\phi^{\mathrm{vp}}$, the variations of stress and the yield function are obtained as:

$$\delta\boldsymbol{\sigma} = \frac{\partial\boldsymbol{\sigma}}{\partial\boldsymbol{\epsilon}} : \delta\boldsymbol{\epsilon} + \frac{\partial\boldsymbol{\sigma}}{\partial p}\delta p + \frac{\partial\boldsymbol{\sigma}}{\partial c^{\mathrm{L}}}\delta c^{\mathrm{L}}, \tag{B.5}$$

where can be expanded as:

$$\delta\boldsymbol{\sigma} = \mathbb{B}^{\mathrm{a}} : \delta\boldsymbol{\epsilon} + \boldsymbol{B}^{\mathrm{b}}\delta p + \boldsymbol{B}^{\mathrm{c}}\delta c^{\mathrm{L}}, \tag{B.6}$$

with

$$\begin{aligned} &\mathbb{B}^{\mathrm{a}} = (1-D)\mathbb{C}^{\mathrm{e}}, && \boldsymbol{B}^{\mathrm{b}} = -(1-D)\mathbb{C}^{\mathrm{e}} : \boldsymbol{\Lambda}^{\mathrm{vp}}, \\ &\boldsymbol{B}^{\mathrm{c}} = -(1-D)\mathbb{C}^{\mathrm{e}} : \boldsymbol{H}, && \boldsymbol{H} = \frac{V^{\mathrm{H}}}{3V^{\mathrm{M}}}\boldsymbol{I}. \end{aligned} \tag{B.7}$$

Similarly, the variation of the yield function is expressed as:

$$\delta f = \boldsymbol{F}_{\boldsymbol{\sigma}} : \delta\boldsymbol{\sigma} + \boldsymbol{F}_{\boldsymbol{\chi}} : \delta\boldsymbol{\chi} + f_{\mathrm{p}}\delta p + f_{\mathrm{D}}\delta D \tag{B.8}$$

with

$$\boldsymbol{F}_{\boldsymbol{\sigma}} = \frac{\partial f}{\partial\boldsymbol{\sigma}}, \quad \boldsymbol{F}_{\boldsymbol{\chi}} = \frac{\partial f}{\partial\boldsymbol{\chi}}, \quad f_{\mathrm{p}} = \frac{\partial f}{\partial p}, \quad f_{\mathrm{D}} = \frac{\partial f}{\partial D}. \tag{B.9}$$

Based on Eq. (B.9), δf can be expressed as:

$$\delta f = \boldsymbol{F}_{\boldsymbol{\sigma}} : (\mathbb{B}^{\mathrm{a}} : \delta\boldsymbol{\epsilon} + \boldsymbol{B}^{\mathrm{b}}\delta p + \boldsymbol{B}^{\mathrm{c}}\delta C^{L}) + \boldsymbol{F}_{\boldsymbol{\chi}} : \delta\boldsymbol{\xi} + f_{\mathrm{p}}\delta p + f_{\mathrm{D}}\Lambda^{\mathrm{D}}\delta p, \tag{B.10}$$

Equation (B.10) can be reformulated as:

$$\delta f = B^{\mathrm{d}} : \delta\boldsymbol{\epsilon} + \boldsymbol{B}^{\mathrm{e}}\delta C^{\mathrm{L}} + \boldsymbol{B}^{\mathrm{f}}\delta p, \tag{B.11}$$

with

$$B^{\mathrm{d}} = \boldsymbol{F_\sigma} : \boldsymbol{B}^{\mathrm{a}}, \quad B^{\mathrm{e}} = \boldsymbol{F_\sigma} : \boldsymbol{B}^{\mathrm{c}}, \quad B^{\mathrm{f}} = \boldsymbol{F_\sigma} : \boldsymbol{B}^{\mathrm{b}} + f_r + f_D\Lambda^{\mathrm{D}} + \boldsymbol{F_\chi} : \boldsymbol{\Lambda}^{\mathrm{bs}}. \tag{B.12}$$

The variation of the viscoplastic criterion, $\delta\phi^{\mathrm{vp}}$ is derived as:

$$\delta\phi^{\mathrm{vp}} = \frac{\partial\phi^{\mathrm{vp}}}{\partial f}\delta f + \frac{\partial\phi^{\mathrm{vp}}}{\partial r}\delta p. \tag{B.13}$$

Substituting Eq. (B.11) into Eq. (B.13) yields:

$$\delta\phi^{\mathrm{vp}} = \Omega^*(B^{\mathrm{d}} : \delta\boldsymbol{\epsilon} + B^{\mathrm{e}}\delta C^{\mathrm{L}} + B^{\mathrm{f}}\delta r) - \frac{1}{\Delta t}\delta, \tag{B.14}$$

with:

$$\Omega^* = P^{\mathrm{vp}}\left(\frac{f+|f|}{2R^{\mathrm{vp}}}\right)^{P^{\mathrm{vp}}-1}\left(\frac{1+\mathrm{sgn}(f)}{2R^{\mathrm{vp}}}\right). \tag{B.15}$$

Equation (B.14) is reorganized as:

$$\delta\phi^{\mathrm{vp}} = \Omega^*\boldsymbol{B}^{\mathrm{d}} : \delta\boldsymbol{\epsilon} + \Omega^* B^{\mathrm{e}}\delta c^{\mathrm{L}} + \left(\Omega^* B^{\mathrm{f}} - \frac{1}{\Delta t}\right)\delta p. \tag{B.16}$$

In each time step, the variations of the total strain, $\delta\boldsymbol{\epsilon}$ and lattice hydrogen, δC^L concentration are considered zero. Thus, the iterative equation (Eq. (B.4)) is derived as:

$$\delta\phi^{\mathrm{vp}} = \left(\Omega^* B^{\mathrm{f}} - \frac{1}{\Delta t}\right)\delta p. \tag{B.17}$$

B.2. Tangent operators

To derive tangent moduli, this time, the variation of viscoplastic criterion is set to zero, and the variations of the total strain and lattice hydrogen concentration are not ignored:

$$\mathrm{d}\phi^{\mathrm{vp}} = \Omega^*\boldsymbol{B}^{\mathrm{d}} : \mathrm{d}\boldsymbol{\epsilon} + \Omega^* B^{\mathrm{e}}\mathrm{d}c^{\mathrm{L}} + \left(\Omega^* B^{\mathrm{f}} - \frac{1}{\Delta t}\right)\mathrm{d}p = 0. \tag{B.18}$$

Using Eq. (B.18), $\mathrm{d}p$ is derived as:

$$\mathrm{d}p = -\frac{\Omega^*\boldsymbol{B}^{\mathrm{d}}}{\left(\Omega^* B^{\mathrm{f}} - \frac{1}{\Delta t}\right)} : \mathrm{d}\boldsymbol{\epsilon} - \frac{\Omega^*\boldsymbol{B}^{\mathbf{e}}}{\left(\Omega^* B^{\mathrm{f}} - \frac{1}{\Delta t}\right)}\mathrm{d}c^{\mathrm{L}}. \tag{B.19}$$

Substituting Eq. (B.19) into Eq. (B.6) yields:

$$\mathrm{d}\boldsymbol{\sigma} = \left(\mathbb{B}^{\mathrm{a}} - \frac{\Omega^* \boldsymbol{B}^{\mathrm{b}} \otimes \boldsymbol{B}^{\mathrm{d}}}{\left(\Omega^* B^{\mathrm{f}} - \frac{1}{\Delta t}\right)}\right) : \mathrm{d}\boldsymbol{\epsilon} + \left(-\frac{\Omega^* B^{\mathrm{e}}}{\left(\Omega^* B^{\mathrm{f}} - \frac{1}{\Delta t}\right)} \boldsymbol{B}^{\mathrm{b}} + \boldsymbol{B}^{\mathrm{c}}\right) \mathrm{d}c^{\mathrm{L}}. \tag{B.20}$$

From Eq. (B.20), the tangent operators, $\mathbb{T}^{\boldsymbol{\sigma}}_{\boldsymbol{\epsilon}}$ and $\mathbb{T}^{\boldsymbol{\sigma}}_{C}$ are derived as:

$$\mathbb{T}^{\boldsymbol{\sigma}}_{\boldsymbol{\epsilon}} = \mathbb{B}^{\mathrm{a}} - \frac{\Omega^* \boldsymbol{B}^{\mathrm{b}} \otimes \boldsymbol{B}^{\mathrm{d}}}{\left(\Omega^* B^{\mathrm{f}} - \frac{1}{\Delta t}\right)}, \qquad \boldsymbol{T}^{\boldsymbol{\sigma}}_{C} = -\frac{\Omega^* B^{\mathrm{e}}}{\left(\Omega^* B^{\mathrm{f}} - \frac{1}{\Delta t}\right)} \boldsymbol{B}^{\mathrm{b}} + \boldsymbol{B}^{\mathrm{c}}. \tag{B.21}$$

Similarly, the hydrogen diffusion equation tangent operators can be derived. To this end, the variation of the hydrogen diffusion equation is expressed as:

$$\frac{\partial}{\partial t}(c^{\mathrm{L}} + c^{\mathrm{T}}) + \boldsymbol{\nabla} \cdot \left[-D^{\mathrm{H}}\left(\boldsymbol{\nabla} c^{\mathrm{L}} + \frac{c^{\mathrm{L}} V^{\mathrm{H}}}{RT} \boldsymbol{\nabla} \sigma^{\mathrm{hyd}}\right)\right] = 0. \tag{B.22}$$

Here, the Hydrogen diffusion related tangent operator is obtained as:

$$T^{\mathrm{H}}_{\mathrm{C}} = -D^{\mathrm{H}}. \tag{B.23}$$

Appendix C. Finite element governing equation

Here, an 8 node 3D brick element is considered. Shape functions are introduced to simplify the integral calculations. Using the shape functions, the equivalent displacement of each element can be calculated considering the related values in the nodes. With this in mind, the element displacement filed, u^{e}, v^{e}, and w^{e}, and the hydrogen concentration, c^{L} are expressed as:

$$\begin{aligned}
u^{\mathbf{e}}(x,y,z,t) &= \sum_{i=1}^{n^{\mathrm{e}}} N_i(x,y,z) u_i(t), \\
v^{\mathbf{e}}(x,y,z,t) &= \sum_{i=1}^{n^{\mathrm{e}}} N_i(x,y,z) v_i(t), \\
w^{\mathbf{e}}(x,y,z,t) &= \sum_{i=1}^{n^{\mathrm{e}}} N_i(x,y,z) w_i(t), \\
c^{\mathrm{L}}(x,y,z,t) &= \sum_{i=1}^{n^{\mathrm{e}}} N_i(x,y,z) c^{\mathrm{L}}_i(t),
\end{aligned} \tag{C.1}$$

where u_i, v_i and w_i are the displacements along X-axis, Y-axis, and Z-axis at i-th node, respectively, and c^{L}_i is the hydrogen concentration at i-th node. Here, t denotes time, and N_i is the shape function corresponding to the i-th

node. Similarly, considering isoparametric interpolation functions, the global coordinates[1] of the geometry are expressed as:

$$\begin{aligned} X(x,y,z,t) &= \sum_{i=1}^{n^{\mathrm{e}}} N_i(x,y,z)X_i(t), \\ Y(x,y,z,t) &= \sum_{i=1}^{n^{\mathrm{e}}} N_i(x,y,z)Y_i(t), \\ Z(x,y,z,t) &= \sum_{i=1}^{n^{\mathrm{e}}} N_i(x,y,z)Z_i(t). \end{aligned} \tag{C.2}$$

It should be noted that in the isoparametric elements, interpolation and shape functions are equal. Interpolation functions are derived through Lagrange interpolation functions, which can be defined for an n^{e} nodes element in general as:

$$L_i(x) = \frac{1}{2}(1+xx_i), \qquad L_j(y) = \frac{1}{2}(1+yy_j), \qquad L_k(z) = \frac{1}{2}(1+zz_j), \tag{C.3}$$

where x_i and x_j are the x coordinates of nodes, and L_i denotes the Lagrange function at the i-th node. The Lagrange function is derived similarly for Y and Z axes also. The interpolation functions are obtained through the multiplication of the interpolation functions based on X, Y, and Z axes. The local coordinates, x, y and z, for simplicity, varies between -1 and 1. With this in mind, the shape functions are defined as:

$$\begin{aligned} N_1 &= \frac{1}{8}(1-x)(1+y)(1-z), \qquad N_2 = \frac{1}{8}(1-x)(1-y)(1-z), \\ N_3 &= \frac{1}{8}(1-x)(1-y)(1+z), \qquad N_4 = \frac{1}{8}(1-x)(1+y)(1+z), \\ N_5 &= \frac{1}{8}(1+x)(1+y)(1-z), \qquad N_6 = \frac{1}{8}(1+x)(1-y)(1-z), \\ N_7 &= \frac{1}{8}(1+x)(1-y)(1+z), \qquad N_8 = \frac{1}{8}(1+x)(1+y)(1+z). \end{aligned} \tag{C.4}$$

The global coordinate derivatives of the shape functions are derived as follows:

$$\begin{aligned} \frac{\partial N_i}{\partial X} &= \frac{\partial N_i}{\partial x}\frac{\partial x}{\partial X} + \frac{\partial N_i}{\partial y}\frac{\partial y}{\partial X} + \frac{\partial N_i}{\partial z}\frac{\partial z}{\partial X}, \\ \frac{\partial N_i}{\partial Y} &= \frac{\partial N_i}{\partial x}\frac{\partial x}{\partial Y} + \frac{\partial N_i}{\partial y}\frac{\partial y}{\partial Y} + \frac{\partial N_i}{\partial z}\frac{\partial z}{\partial Y}, \\ \frac{\partial N_i}{\partial Z} &= \frac{\partial N_i}{\partial x}\frac{\partial x}{\partial Z} + \frac{\partial N_i}{\partial y}\frac{\partial y}{\partial Z} + \frac{\partial N_i}{\partial z}\frac{\partial z}{\partial Z}. \end{aligned} \tag{C.5}$$

[1]Global coordinates: the values determined at the level of the entire structure. Local coordinates: the coordinates at the element level.

The local coordinate derivatives of the shape functions are derived as follows:

$$\begin{aligned}\frac{\partial N_i}{\partial x} &= \frac{\partial N_i}{\partial X}\frac{\partial X}{\partial x} + \frac{\partial N_i}{\partial Y}\frac{\partial Y}{\partial x} + \frac{\partial N_i}{\partial Z}\frac{\partial Z}{\partial x},\\ \frac{\partial N_i}{\partial y} &= \frac{\partial N_i}{\partial X}\frac{\partial X}{\partial y} + \frac{\partial N_i}{\partial Y}\frac{\partial Y}{\partial y} + \frac{\partial N_i}{\partial Z}\frac{\partial Z}{\partial y},\\ \frac{\partial N_i}{\partial z} &= \frac{\partial N_i}{\partial X}\frac{\partial x}{\partial z} + \frac{\partial N_i}{\partial y}\frac{\partial y}{\partial z} + \frac{\partial N_i}{\partial z}\frac{\partial z}{\partial z},\end{aligned} \tag{C.6}$$

where can be written as:

$$\begin{Bmatrix} \frac{\partial N_i}{\partial x} \\ \frac{\partial N_i}{\partial y} \\ \frac{\partial N_i}{\partial z} \end{Bmatrix} = \begin{bmatrix} \frac{\partial X}{\partial x} & \frac{\partial Y}{\partial x} & \frac{\partial Z}{\partial x} \\ \frac{\partial X}{\partial y} & \frac{\partial Y}{\partial y} & \frac{\partial Z}{\partial y} \\ \frac{\partial X}{\partial z} & \frac{\partial Y}{\partial z} & \frac{\partial Z}{\partial z} \end{bmatrix} \begin{Bmatrix} \frac{\partial N_i}{\partial X} \\ \frac{\partial N_i}{\partial Y} \\ \frac{\partial N_i}{\partial Z} \end{Bmatrix} = \boldsymbol{j} \begin{Bmatrix} \frac{\partial N_i}{\partial X} \\ \frac{\partial N_i}{\partial Y} \\ \frac{\partial N_i}{\partial Z} \end{Bmatrix}, \tag{C.7}$$

where $\boldsymbol{J}$ denotes the Jacobian matrix, based on which the global coordinate derivatives are derived as:

$$\boldsymbol{j} = \begin{bmatrix} \frac{\partial X}{\partial x} & \frac{\partial Y}{\partial y} & \frac{\partial Z}{\partial x} \\ \frac{\partial X}{\partial y} & \frac{\partial Y}{\partial y} & \frac{\partial Z}{\partial y} \\ \frac{\partial X}{\partial z} & \frac{\partial Y}{\partial z} & \frac{\partial Z}{\partial z} \end{bmatrix} = \begin{bmatrix} \sum_{i=1}^{n^{\mathrm{e}}} \frac{\partial N_i}{\partial x} X_i & \sum_{i=1}^{n^{\mathrm{e}}} \frac{\partial N_i}{\partial x} Y_i & \sum_{i=1}^{n^{\mathrm{e}}} \frac{\partial N_i}{\partial x} Z_i \\ \sum_{i=1}^{n^{\mathrm{e}}} \frac{\partial N_i}{\partial y} X_i & \sum_{i=1}^{n^{\mathrm{e}}} \frac{\partial N_i}{\partial y} Y_i & \sum_{i=1}^{n^{\mathrm{e}}} \frac{\partial N_i}{\partial y} Z_i \\ \sum_{i=1}^{n^{\mathrm{e}}} \frac{\partial N_i}{\partial z} X_i & \sum_{i=1}^{n^{\mathrm{e}}} \frac{\partial N_i}{\partial z} Y_i & \sum_{i=1}^{n^{\mathrm{e}}} \frac{\partial N_i}{\partial z} Z_i \end{bmatrix}. \tag{C.8}$$

The strain tensor using the Voigt notation, for a 3D case, based on the infinitesimal strain theory, is expressed as:

$$\boldsymbol{\epsilon}^{\mathbf{e}} = \begin{Bmatrix} \epsilon_{xx} \\ \epsilon_{yy} \\ \epsilon_{zz} \\ \gamma_{xy} = 2\epsilon_{xy} \\ \gamma_{yz} = 2\epsilon_{yz} \\ \gamma_{xz} = 2\epsilon_{xz} \end{Bmatrix} = \begin{Bmatrix} \frac{\partial u^{\mathrm{e}}}{\partial x} \\ \frac{\partial v^{\mathrm{e}}}{\partial y} \\ \frac{\partial w^{\mathrm{e}}}{\partial z} \\ \left(\frac{\partial u^{\mathrm{e}}}{\partial y} + \frac{\partial v^{\mathrm{e}}}{\partial x}\right) \\ \left(\frac{\partial v^{\mathrm{e}}}{\partial z} + \frac{\partial w^{\mathrm{e}}}{\partial y}\right) \\ \left(\frac{\partial u^{\mathrm{e}}}{\partial z} + \frac{\partial w^{\mathrm{e}}}{\partial x}\right) \end{Bmatrix} \tag{C.9}$$

$$= \left\{ \begin{array}{c} \displaystyle\sum_{i=1}^{n^{\mathrm{e}}} \frac{\partial N_i\,(x,y,z)}{\partial x} u_i(t) \\ \displaystyle\sum_{i=1}^{n^{\mathrm{e}}} \frac{\partial N_i\,(x,y,z)}{\partial y} v_i(t) \\ \displaystyle\sum_{i=1}^{n^{\mathrm{e}}} \frac{\partial N_i\,(x,y,z)}{\partial z} w_i(t) \\ \displaystyle\sum_{i=1}^{n^{\mathrm{e}}} \left(\frac{\partial N_i\,(x,y,z)}{\partial y} u_i\,(t) + \frac{\partial N_i\,(x,y,z)}{\partial x} v_i(t) \right) \\ \displaystyle\sum_{i=1}^{n^{\mathrm{e}}} \left(\frac{\partial N_i\,(x,y,z)}{\partial z} v_i\,(t) + \frac{\partial N_i\,(x,y,z)}{\partial y} w_i(t) \right) \\ \displaystyle\sum_{i=1}^{n^{\mathrm{e}}} \left(\frac{\partial N_i\,(x,y,z)}{\partial z} u_i\,(t) + \frac{\partial N_i\,(x,y,z)}{\partial x} w_i(t) \right) \end{array} \right\}.$$

Thus, the strain tensor can be derived based on the displacement and derivative of shape functions as follows:

$$\boldsymbol{\epsilon}^{\mathbf{e}} = [\, \boldsymbol{B}_1 \; \ldots \; \boldsymbol{B}_i \; \ldots \; \boldsymbol{B}_{n^e} \,] \left\{ \begin{array}{c} u_1 \\ v_1 \\ w_1 \\ \vdots \\ u_{n^{\mathrm{e}}} \\ v_{n^{\mathrm{e}}} \\ w_{n^{\mathrm{e}}} \end{array} \right\} \tag{C.10}$$

with

$$\boldsymbol{B}_i = \left[\begin{array}{ccc} \dfrac{\partial N_i(x,y,z)}{\partial x} & 0 & 0 \\ 0 & \dfrac{\partial N_i(x,y,z)}{\partial y} & 0 \\ 0 & 0 & \dfrac{\partial N_i(x,y,z)}{\partial z} \\ \dfrac{\partial N_i(x,y,z)}{\partial y} & \dfrac{\partial N_i(x,y,z)}{\partial x} & 0 \\ 0 & \dfrac{\partial N_i(x,y,z)}{\partial z} & \dfrac{\partial N_i(x,y,z)}{\partial y} \\ \dfrac{\partial N_i(x,y,z)}{\partial z} & 0 & \dfrac{\partial N_i(x,y,z)}{\partial x} \end{array} \right].$$

Similarly, $\boldsymbol{\nabla} C^{\mathrm{L}}$ is derived as:

$$\text{(C.11)}\quad \boldsymbol{\nabla} C^{\mathrm{L}} = \left[\, \boldsymbol{B}_1^{\mathrm{C}} \;\ldots\; \boldsymbol{B}_i^{\mathrm{C}} \;\ldots\; \boldsymbol{B}_{n^{\mathrm{e}}}^{\mathrm{C}} \,\right] \begin{Bmatrix} c_1^{\mathrm{L}} \\ c_2^{\mathrm{L}} \\ c_3^{\mathrm{L}} \\ \vdots \\ c_{n^{\mathrm{e}}}^{\mathrm{L}} \end{Bmatrix} \quad \text{with } \boldsymbol{B}_i^{C} = \begin{bmatrix} \dfrac{\partial N_i(x,y,z)}{\partial x} \\ \dfrac{\partial N_i(x,y,z)}{\partial y} \\ \dfrac{\partial N_i(x,y,z)}{\partial z} \end{bmatrix}.$$

C.1. Stress equilibrium FE implementation

To solve a static mechanical problem, the stress equilibrium considering the corresponding boundary condition is solved. For an arbitrary domain, as Ω with the boundary of $\partial\Omega$. The stress equilibrium in the differential representation can be presented as:

$$\text{(C.12)}\qquad \boldsymbol{\nabla}\cdot\boldsymbol{\sigma} + \boldsymbol{f}_{\mathbf{b}} = 0 \;\forall x \in \Omega \quad \text{with } \boldsymbol{\sigma}\cdot\boldsymbol{n} = \boldsymbol{f}_{\mathrm{s}} \;\forall x \in \partial\Omega.$$

The integral form based on the virtual work principle is expressed as:

$$\text{(C.13)}\qquad \int_{\Omega} \boldsymbol{\sigma} : \delta_u \boldsymbol{\epsilon}\,\mathrm{d}V - \int_{\Omega} \boldsymbol{f}_{\mathrm{b}}\cdot\delta\boldsymbol{u}\,\mathrm{d}V - \int_{\partial\Omega} \boldsymbol{f}_{\mathrm{s}}\cdot\delta\boldsymbol{u}\,\mathrm{d}S = 0.$$

The right-hand side vector in the mechanical equation is derived as:

$$\text{(C.14)}\qquad r_i^M = \int_{\Omega} (\boldsymbol{B}_i^{\mathrm{T}} : \mathbb{C} : \boldsymbol{\epsilon} - N_i^{\mathrm{T}}\boldsymbol{f}_{\mathrm{b}})\,\mathrm{d}V - \int_{\partial\Omega} N_i^{\mathrm{T}}\boldsymbol{f}_{\mathrm{s}}\,\mathrm{d}S.$$

Based on the above equations, the mechanical tangent modulus is obtained as:

$$\text{(C.15)}\qquad \mathbf{K}_{\boldsymbol{ij}}^{\boldsymbol{uu}} = \int_{\Omega} (\boldsymbol{B}_i^{\mathrm{T}} : \mathbb{C} : \boldsymbol{B}_j)\,\mathrm{d}V.$$

C.2. Diffusion equation FE implementation

The integral form of the diffusion equation with a slight variation of the hydrogen concentration, δC, can be expressed as:

$$\text{(C.16)}\qquad \int_V \delta\mu \Bigg(\left(\frac{c^{\mathrm{L}} + c^{\mathrm{T}}(1-\theta^{\mathrm{T}})}{c^L} \right) \frac{\partial c^{\mathrm{L}}}{\partial t} + \alpha^{\mathrm{H}}\theta^{\mathrm{T}} \frac{\partial N^{\mathrm{T}}}{\partial p}\,\frac{\partial p}{\partial t} + \boldsymbol{\nabla}\cdot\left[-D^{\mathrm{H}} \left(\boldsymbol{\nabla} C^{\mathrm{L}} - \frac{c^{\mathrm{L}} V^{\mathrm{H}}}{RT} \boldsymbol{\nabla}\sigma^{\mathrm{hyd}} \right) \right] \Bigg)\,\mathrm{d}V = 0.$$

Using the divergence theorem, Eq. (C.16) is expressed as:

$$\int_{\Omega}\left(\delta C^{\mathrm{L}}\left(\frac{c^{\mathrm{L}}+c^{\mathrm{T}}(1-\theta^{\mathrm{T}})}{c^{\mathrm{L}}}\right)\frac{\partial c^{\mathrm{L}}}{\partial t}+\delta c^{\mathrm{L}}\alpha^{\mathrm{H}}\theta^{\mathrm{T}}\frac{\partial N^{\mathrm{T}}}{\partial p}\frac{\partial p}{\partial t}\right.$$
$$\left.-\left[-D^{\mathrm{H}}\left(\boldsymbol{\nabla}c^{\mathrm{L}}-\frac{c^{\mathrm{L}}V^{\mathrm{H}}}{RT}\boldsymbol{\nabla}\sigma^{\mathrm{hyd}}\right)\right]\cdot\boldsymbol{\nabla}\delta c^{\mathrm{L}}\right)\mathrm{d}V$$
$$+\int_{\partial\Omega}\left[-D^{\mathrm{H}}\left(\boldsymbol{\nabla}c^{\mathrm{L}}-\frac{c^{\mathrm{L}}V^{\mathrm{H}}}{RT}\boldsymbol{\nabla}\sigma^{\mathrm{hyd}}\right)\right]\delta c^{\mathrm{L}}\cdot\boldsymbol{n}\,\mathrm{d}S=0. \tag{C.17}$$

Using Eq. (C.17), the following equation is derived:

$$\int_{\Omega}\left(\delta C^{\mathrm{L}}\left(\frac{c^{\mathrm{L}}+c^{\mathrm{T}}(1-\theta^{T})}{c^{\mathrm{L}}}\right)\frac{1}{D^{\mathrm{H}}}\frac{\partial c^{\mathrm{L}}}{\partial t}+\delta c^{\mathrm{L}}\alpha^{\mathrm{H}}\theta^{\mathrm{T}}\frac{\partial N^{\mathrm{T}}}{\partial p}\frac{1}{D^{\mathrm{L}}}\frac{\partial p}{\partial t}\right.$$
$$\left.+\boldsymbol{\nabla}c^{\mathrm{L}}\cdot\boldsymbol{\nabla}\delta c^{\mathrm{L}}-\frac{c^{\mathrm{L}}V^{\mathrm{H}}}{RT}\boldsymbol{\nabla}\sigma^{\mathrm{hyd}}\cdot\boldsymbol{\nabla}\delta c^{\mathrm{L}}\right)\mathrm{d}V$$
$$=\int_{\partial\Omega}\left[\boldsymbol{\nabla}c^{\mathrm{L}}-\frac{c^{\mathrm{L}}V^{\mathrm{H}}}{RT}\boldsymbol{\nabla}\sigma^{\mathrm{hyd}}\right]\delta c^{\mathrm{L}}\cdot\boldsymbol{n}\,\mathrm{d}S. \tag{C.18}$$

The right-hand side vector, using the shape functions, can be expressed as:

$$r_i^{\mathrm{c}}=\int_{\Omega}\left(N_i\left[\frac{1}{D^{\mathrm{H}}}\left(\frac{c^{\mathrm{L}}+c^{\mathrm{T}}(1-\theta^{\mathrm{T}})}{c^{\mathrm{L}}}\right)\frac{\partial c^{\mathrm{L}}}{\partial t}+\alpha^{\mathrm{H}}\theta^{\mathrm{T}}\frac{\partial N^{\mathrm{T}}}{\partial p}\frac{1}{D^{\mathrm{H}}}\frac{\partial p}{\partial t}\right]\right.$$
$$\left.+\boldsymbol{B}_{\mathrm{i}}^{\mathrm{c(T)}}\boldsymbol{\nabla}c^{\mathrm{L}}-\frac{c^{\mathrm{L}}V^{\mathrm{H}}}{RT}\boldsymbol{\nabla}\sigma^{\mathrm{hyd}}\cdot\boldsymbol{B}_{\mathrm{i}}^{\mathrm{C}}\right)\mathrm{d}V-\int_{\partial\Omega}N_i\left[\boldsymbol{\nabla}c^{L}-\frac{c^{\mathrm{L}}V^{\mathrm{H}}}{RT}\boldsymbol{\nabla}\sigma^{\mathrm{hyd}}\right]\cdot\boldsymbol{n}\,\mathrm{d}S. \tag{C.19}$$

The diffusional tangent modulus is derived as:

$$K_{ij}^{\mathrm{CC}}=\int_{\Omega}\left(\boldsymbol{B}_{\mathrm{i}}^{\mathrm{C(T)}}\boldsymbol{B}_{j}^{\mathrm{C}}-\boldsymbol{B}_{\mathrm{i}}^{\mathrm{C(T)}}\frac{V^{\mathrm{H}}}{RT}\boldsymbol{\nabla}\sigma^{\mathrm{hyd}}N_j\right)\mathrm{d}V. \tag{C.20}$$

The hydrostatic, σ^{hyd}, stress is calculated at the element level. At each integration point, the hydrostatic stress is calculated as:

$$\sigma^{\mathrm{hyd}}=\sum_{k=1}^{n^{\mathrm{e}}}\sigma_i^{\mathrm{hyd}}N_k(x,y,z). \tag{C.21}$$

Thus, the hydrostatic stress gradient for the element is derived as:

$$\boldsymbol{\nabla}\sigma^{\mathrm{hyd}}=\sum_{k=1}^{n^{\mathrm{e}}}\boldsymbol{B}_k^{\mathrm{C}}\sigma_k^{\mathrm{hyd}}. \tag{C.22}$$

To include the hydrogen concentration rate, another global matrix, $\boldsymbol{F}$ is considered, the concentration-related component is derived as:

$$M_{ij}^{\mathrm{CC}} = \int_{\Omega} \left(N_i \frac{1}{D^{\mathrm{H}}} \left[\left(\frac{\sum_{k=1}^{n^{\mathrm{e}}} c_k^{\mathrm{L}} N^k + \mathrm{c}^{\mathrm{T}}(1-\theta^{\mathrm{T}})}{\sum_{k=1}^{n^e} c_k^{\mathrm{L}} N^k} \right) \right] N_j \right) \mathrm{d}V. \tag{C.23}$$

Considering the flux, $\boldsymbol{q}^0$, at the boundaries, the last integral term on the domain boundary appeared in the FE components as:

$$b_i^{\mathrm{C}} = \int_{\Omega} N_i \boldsymbol{q}^0 \cdot \boldsymbol{n} \, \mathrm{d}S. \tag{C.24}$$

There is also a term in function of the equivalent plastic strain rate derived as:

$$g_i^C = \int_{\Omega} \int_{\Omega} N_i \alpha^{\mathrm{H}} \theta^{\mathrm{T}} \frac{\partial N^{\mathrm{T}}}{\partial p} \frac{1}{D^{\mathrm{H}}} \frac{\partial p}{\partial t} \, \mathrm{d}V. \tag{C.25}$$

C.3. Coupled mechanical-diffusional FE equations

The equations discretized and linearized above are written in a coupled form as following:

$$\begin{bmatrix} \boldsymbol{K}^{\mathrm{uu}} & \boldsymbol{0} \\ \boldsymbol{0} & \boldsymbol{K}^{\mathrm{CC}} \end{bmatrix} \begin{Bmatrix} \boldsymbol{u} \\ \mathbf{C} \end{Bmatrix} + \begin{bmatrix} \boldsymbol{0} & \boldsymbol{0} \\ \boldsymbol{0} & \boldsymbol{M}^{\mathrm{CC}} \end{bmatrix} \begin{Bmatrix} \dot{\boldsymbol{u}} \\ \dot{\boldsymbol{c}} \end{Bmatrix} = \begin{Bmatrix} \boldsymbol{b}^{\mathrm{u}} \\ \boldsymbol{b}^{\mathrm{C}} \end{Bmatrix} - \begin{Bmatrix} \boldsymbol{0} \\ \boldsymbol{g}^{\mathrm{C}} \end{Bmatrix}. \tag{C.26}$$

The above equation is solved using the Newton–Raphson method. To this end the residual is defined as:

$$\begin{aligned} \boldsymbol{\phi}^{\mathrm{r}} = & \begin{bmatrix} \mathbf{K}^{\mathrm{uu}} & \boldsymbol{0} \\ \boldsymbol{0} & \boldsymbol{K}^{\mathrm{CC}} \end{bmatrix} \begin{Bmatrix} \boldsymbol{u}_{n+1} \\ \boldsymbol{c}_{n+1} \end{Bmatrix} \\ & + \frac{1}{\Delta t} \begin{bmatrix} \boldsymbol{0} & \boldsymbol{0} \\ \boldsymbol{0} & \boldsymbol{M}^{\mathrm{CC}} \end{bmatrix} \left(\begin{Bmatrix} \boldsymbol{u}_{n+1} \\ \boldsymbol{c}_{n+1} \end{Bmatrix} - \begin{Bmatrix} \boldsymbol{u}_n \\ \boldsymbol{c}_n \end{Bmatrix} \right) - \begin{Bmatrix} \boldsymbol{b}^{\mathrm{u}} \\ \boldsymbol{b}^{\mathrm{C}} \end{Bmatrix} + \begin{Bmatrix} \boldsymbol{0} \\ \boldsymbol{g}^{\mathrm{C}} \end{Bmatrix} \\ & = \boldsymbol{0}. \end{aligned} \tag{C.27}$$

The iterative equation is derived as follows:

$$\begin{Bmatrix} \boldsymbol{u}_{n+1}^{k+1} \\ \boldsymbol{c}_{n+1}^{k+1} \end{Bmatrix} = \begin{Bmatrix} \boldsymbol{u}_{n+1}^{k} \\ \boldsymbol{c}_{n+1}^{k} \end{Bmatrix} - \boldsymbol{J}^{*^{-1}} \boldsymbol{\phi}^{\mathrm{r}^k}, \tag{C.28}$$

with:

$$\boldsymbol{J}^* = \left[\begin{bmatrix} \boldsymbol{K}^{\mathrm{uu}} & \boldsymbol{0} \\ \boldsymbol{0} & \boldsymbol{K}^{\mathrm{CC}} \end{bmatrix} + \frac{1}{\Delta t} \begin{bmatrix} \boldsymbol{0} & \boldsymbol{0} \\ \boldsymbol{0} & \boldsymbol{M}^{\mathrm{CC}} \end{bmatrix} \right]. \tag{C.29}$$

For numerical stability and implementation simplicity, the present finite element implementation uses a staggered solution strategy. Therefore, the mechanical equilibrium equation and the hydrogen diffusion equation are not solved in a fully monolithic Newton system, and the global tangent blocks are not explicitly assembled. At each time increment, the diffusion equation is first solved to update the lattice hydrogen concentration. The mechanical problem is then solved using the updated hydrogen field, followed by the update of the state variables at the integration points. Thus, the coupling is introduced through the sequential update of hydrogen transport, trapping, viscoplasticity, and ductile damage. The numerical stability of the staggered procedure is checked by monitoring the maximum lattice hydrogen concentration, hydrostatic stress, von Mises stress, accumulated plastic strain, and damage variable during the simulations.

Acknowledgements

We sincerely thank Capgemini Engineering for their generous support. Their financial help and resources were key to completing this study.

References

1. K. Wróbel, J. Wróbel, W. Tokarz, J. Lach, K. Podsadni, A. Czerwiński, *Hydrogen internal combustion engine vehicles: A review*, Energies, **15**, 8937, 2022, https://doi.org/10.3390/en15238937.
2. M. Handwerker, J. Wellnitz, H. Marzbani, *Comparison of hydrogen powertrains with the battery powered electric vehicle and investigation of small-scale local hydrogen production using renewable energy*, Hydrogen, **2**, 76–100, 2021, https://doi.org/10.3390/hydrogen2010005.
3. S. Falfari, G. Cazzoli, V. Mariani, G.M. Bianchi, *Hydrogen application as a fuel in internal combustion engines*, Energies, **16**, 2545, 2023, https://doi.org/10.3390/en16062545.
4. R. Babayev, H.G. Im, A. Andersson, B. Johansson, *Hydrogen double compression-expansion engine (H2DCEE): A sustainable internal combustion engine with 60%+ brake thermal efficiency potential at 45 bar BMEP*, Energy Conversion and Management, **264**, 115698, 2022, https://doi.org/10.1016/j.enconman.2022.115698.
5. W.Y. Choo, J.Y. Lee, *Thermal analysis of trapped hydrogen in pure iron*, Metallurgical Transactions A, **13**, 135–140, 1982, https://doi.org/10.1007/BF02642424.
6. T. Depover, D. Pérez Escobar, E. Wallaert, Z. Zermout, K. Verbeken, *Effect of hydrogen charging on the mechanical properties of advanced high strength steels*, International Journal of Hydrogen Energy, **39**, 4647–4656, 2014, https://doi.org/10.1016/j.ijhydene.2013.12.190.
7. A.J. Kumnick, H.H. Johnson, *Deep trapping states for hydrogen in deformed iron*, Acta Metallurgica, **28**, 33–39, 1980, https://doi.org/10.1016/0001-6160(80)90038-3.

8. M.B. DJUKIC, G.M. BAKIC, V.S. ZERAVCIC, A. SEDMAK, B. RAJICIC, *The synergistic action and interplay of hydrogen embrittlement mechanisms in steels and iron: Localized plasticity and decohesion*, Engineering Fracture Mechanics, **216**, 106528, 2019, https://doi.org/10.1016/j.engfracmech.2019.106528.

9. Y. LI, K. ZHANG, *Analysis of hydrogen-assisted brittle fracture using phase-field damage modelling considering hydrogen enhanced decohesion mechanism*, Metals, **12**, 1032, 2022, https://doi.org/10.3390/met12061032.

10. P. SOFRONIS, Y. LIANG, N. ARAVAS, *Hydrogen induced shear localization of the plastic flow in metals and alloys*, European Journal of Mechanics – A/Solids, **20**, 857–872, 2001, https://doi.org/10.1016/S0997-7538(01)01179-2.

11. YA.S. PODSTRIGACH, V.S. PAVLINA, *Differential equations of thermodynamic processes in n-component solid solutions*, Materials Science, **1**, 259–264, 1966, https://doi.org/10.1007/BF00714880.

12. YA.S. PODSTRIGACH, P.R. SHEVCHUK, *Diffusion phenomena and stress relaxation in the vicinity of a spherical void*, Materials Science, **4**, 140–145, 1969, https://doi.org/10.1007/BF00715566.

13. F. LARCHÉ, J.W. CAHN, *A linear theory of thermochemical equilibrium of solids under stress*, Acta Metallurgica, **21**, 1051–1063, 1973, https://doi.org/10.1016/0001-6160(73)90021-7.

14. A. VILLANI, E.P. BUSSO, K. AMMAR, S. FOREST, M.G.D. GEERS, *A fully coupled diffusional-mechanical formulation: Numerical implementation, analytical validation, and effects of plasticity on equilibrium*, Archive of Applied Mechanics, **84**, 1647–1664, 2014, https://doi.org/10.1007/s00419-014-0860-z.

15. L. ANAND, *A thermo-mechanically-coupled theory accounting for hydrogen diffusion and large elastic–viscoplastic deformations of metals*, International Journal of Solids and Structures, **48**, 962–971, 2011, https://doi.org/10.1016/j.ijsolstr.2010.11.029.

16. P. SOFRONIS, R.M. MCMEEKING, *Numerical analysis of hydrogen transport near a blunting crack tip*, Journal of the Mechanics and Physics of Solids, **37**, 317–350, 1989, https://doi.org/10.1016/0022-5096(89)90002-1.

17. A.H.M. KROM, R.W.J. KOERS, A. BAKKER, *Hydrogen transport near a blunting crack tip*, Journal of the Mechanics and Physics of Solids, **47**, 971–992, 1999, https://doi.org/10.1016/S0022-5096(98)00064-7.

18. Y. CHARLES, J. MOUGENOT, M. GASPÉRINI, *Effect of transient trapping on hydrogen transport near a blunting crack tip*, International Journal of Hydrogen Energy, **46**, 10995–11003, 2021, https://doi.org/10.1016/j.ijhydene.2020.12.155.

19. R. DEPRAETERE, W. DE WAELE, S. HERTELÉ, *Fully-coupled continuum damage model for simulation of plasticity dominated hydrogen embrittlement mechanisms*, Computational Materials Science, **200**, 110857, 2021, https://doi.org/10.1016/j.commatsci.2021.110857.

20. L. JEMBLIE, V. OLDEN, O.M. AKSELSEN, *A coupled diffusion and cohesive zone modelling approach for numerically assessing hydrogen embrittlement of steel structures*, International Journal of Hydrogen Energy, **42**, 11980–11995, 2017, https://doi.org/10.1016/j.ijhydene.2017.02.211.

21. D. LI, R.P. GANGLOFF, J.R. SCULLY, *Hydrogen trap states in ultrahigh-strength AERMET 100 steel*, Metallurgical and Materials Transactions A, **35**, 849–864, 2004, https://doi.org/10.1007/s11661-004-0011-1.

22. P. NOVAK, R. YUAN, B.P. SOMERDAY, P. SOFRONIS, R.O. RITCHIE, *A statistical, physical-based, micro-mechanical model of hydrogen-induced intergranular fracture in steel*, Journal of the Mechanics and Physics of Solids, **58**, 206–226, 2010, https://doi.org/10.1016/j.jmps.2009.10.005.

23. R.A. ORIANI, *The diffusion and trapping of hydrogen in steel*, Acta Metallurgica, **18**, 147–157, 1970, https://doi.org/10.1016/0001-6160(70)90078-7.

24. A. TURNBULL, R.B. HUTCHINGS, D.H. FERRISS, *Modelling of thermal desorption of hydrogen from metals*, Materials Science and Engineering: A, **238**, 317–328, 1997, https://doi.org/10.1016/S0921-5093(97)00426-7.

25. J.P. HIRTH, *Effects of hydrogen on the properties of iron and steel*, Metallurgical Transactions A, **11**, 861–890, 1980, https://doi.org/10.1007/BF02654700.

26. S. HUANG, Y. ZHANG, C. YANG, H. HU, *Fracture strain model for hydrogen embrittlement based on hydrogen enhanced localized plasticity mechanism*, International Journal of Hydrogen Energy, **45**, 25541–25554, 2020, https://doi.org/10.1016/j.ijhydene.2020.06.271.

27. Y. TATEYAMA, T. OHNO, *Stability and clusterization of hydrogen-vacancy complexes in α-Fe: An ab initio study*, Physical Review B, **67**, 174105, 2003, https://doi.org/10.1103/PhysRevB.67.174105.

28. G. ÁLVAREZ MORALES, J. SÁNCHEZ MONTERO, J. SEGURADO ESCUDERO, P. DE ANDRES RODRÍGUEZ, Á. RIDRUEJO RODRÍGUEZ, *Hydrogen diffusion in BCC-Fe: DFT study of tensorial stress effects and interactions with point defects*, Results in Physics, **59**, 107590, 2024, https://doi.org/10.1016/j.rinp.2024.107590.

29. P. SOFRONIS, *The influence of mobility of dissolved hydrogen on the elastic response of a metal*, Journal of the Mechanics and Physics of Solids, **43**, 1385–1407, 1995, https://doi.org/10.1016/0022-5096(95)00037-J.

30. J. LEMAITRE, J.-L. CHABOCHE, *Mechanics of Solid Materials*, 1st paperback ed. (reprint, digitally printed), Cambridge University Press, Cambridge, 2012, https://doi.org/10.1017/CBO9781139167970.

31. L. THIERCELIN, F. PRAUD, F. MERAGHNI, E. FLEURY, *Thermally-activated hardening recovery in viscoplastic materials with kinematic hardening at high temperatures*, Mechanics of Materials, **180**, 104636, 2023, https://doi.org/10.1016/j.mechmat.2023.104636.

32. R.A. ARMSTRONG, *An examination of the concept of "self-evidence" in Thomistic natural law teaching*, [in:] Primary and Secondary Precepts in Thomistic Natural Law Teaching, Springer Netherlands, Dordrecht, 1966, pp. 24–55, https://doi.org/10.1007/978-94-011-9388-7_2.

33. J.L. CHABOCHE, *A review of some plasticity and viscoplasticity constitutive theories*, International Journal of Plasticity, **24**, 1642–1693, 2008, https://doi.org/10.1016/j.ijplas.2008.03.009.

34. J.-L. CHABOCHE, D. NOUAILHAS, *A unified constitutive model for cyclic viscoplasticity and its applications to various stainless steels*, Journal of Engineering Materials and Technology, **111**, 4, 424–430, 1989, https://doi.org/10.1115/1.3226490.

35. M.A. MORETTI, L.-E. LINDGREN, P. ÅKERSTRÖM, *Physics-based flow stress model for alloy 718*, Metallurgical and Materials Transactions A, **54**, 1985–1997, 2023, https://doi.org/10.1007/s11661-022-06819-7.

36. J.A. NELDER, R. MEAD, *A simplex method for function minimization*, The Computer Journal, **7**, 308–313, 1965, https://doi.org/10.1093/comjnl/7.4.308.

37. S. SINGER, J. NELDER, *Nelder–Mead algorithm*, Scholarpedia, **4**, 7, 2928, 2009, https://doi.org/10.4249/scholarpedia.2928.

38. A. AMBROZIAK, *Identification and validation of damage parameters for elasto-viscoplastic Chaboche model*, Engineering Transactions, **55**, 1, 3–28, 2007, https://doi.org/10.24423/engtrans.228.2007

39. G. AMMAR, J. DUFAILLY, *Identification and validation of viscoplastic and damage constitutive equations*, European Journal of Mechanics, A/Solids, **12**, 197, 1993.

40. L. CAO, X. YUAN, *Study on the numerical simulation of the SLM molten pool dynamic behavior of a nickel-based superalloy on the workpiece scale*, Materials, **12**, 2272, 2019, https://doi.org/10.3390/ma12142272.

41. M. KANG, H. GAO, J. WANG, L. LING, B. SUN, *Prediction of microporosity in complex thin-wall castings with the dimensionless Niyama criterion*, Materials, **6**, 1789–1802, 2013, https://doi.org/10.3390/ma6051789.

42. X. LI, J. ZHANG, Q. FU, E. AKIYAMA, X. SONG, Y. WANG, Q. LI, N. ZOU, *Tensile mechanical properties and fracture behaviors of nickel-based superalloy 718 in the presence of hydrogen*, International Journal of Hydrogen Energy, **43**, 20118–20132, 2018, https://doi.org/10.1016/j.ijhydene.2018.08.179.

43. R. DEPRAETERE, W. DE WAELE, M. CAUWELS, T. DEPOVER, K. VERBEKEN, M. BOONE, S. HERTELÉ, *Influence of stress triaxiality on hydrogen assisted ductile damage in an X70 pipeline steel*, Materials Science and Engineering: A, **864**, 144549, 2023, https://doi.org/10.1016/j.msea.2022.144549.

44. K.-W. SEO, Y.-J. KIM, J.-H. HWANG, K.-S. KIM, *Finite element simulation method for combined ductile-brittle fracture of small punch test in hydrogen*, Engineering Fracture Mechanics, **289**, 109489, 2023, https://doi.org/10.1016/j.engfracmech.2023.109489.

45. P.K. KRISTENSEN, C.F. NIORDSON, E. MARTÍNEZ-PAÑEDA, *A phase field model for elastic-gradient-plastic solids undergoing hydrogen embrittlement*, Journal of the Mechanics and Physics of Solids, **143**, 104093, 2020, https://doi.org/10.1016/j.jmps.2020.104093.

46. S. SATOURI, G. CHATZIGEORGIOU, A. BENAARBIA, F. MERAGHNI, *A gradient enhanced constitutive framework for the investigation of ductile damage localization within semicrystalline polymers*, International Journal of Damage Mechanics, **31**, 10, 1639–1675, 2022, https://doi.org/10.1177/10567895221115459.

47. S. SATOURI, G. CHATZIGEORGIOU, A. BENAARBIA, F. MERAGHNI, *Gradient enhanced multi-scale modeling framework for glass fiber reinforced polyamides*, International Journal of Solids and Structures, **267**, 112143, 2023, https://doi.org/10.1016/j.ijsolstr.2023.112143.

48. J.-L. CHABOCHE, *Cyclic viscoplastic constitutive equations, Part I: A thermodynamically consistent formulation*, Journal of Applied Mechanics, **60**, 813–821, 1993, https://doi.org/10.1115/1.2900988.

49. H. KOTAKE, R. MATSUMOTO, S. TAKETOMI, N. MIYAZAKI, *Transient hydrogen diffusion analyses coupled with crack-tip plasticity under cyclic loading*, International Journal of Pressure Vessels and Piping, **85**, 540–549, 2008, https://doi.org/10.1016/j.ijpvp.2008.02.002.

50. F. CHINESTA, A. LEYGUE, F. BORDEU, J.V. AGUADO, E. CUETO, D. GONZALEZ, I. ALFARO, A. AMMAR, A. HUERTA, *PGD-based computational vademecum for efficient design, optimization and control*, Archives of Computational Methods in Engineering, **20**, 31–59, 2013, https://doi.org/10.1007/s11831-013-9080-x.

51. M. EL FALLAKI IDRISSI, F. PRAUD, V. CHAMPANEY, F. CHINESTA, F. MERAGHNI, *Multiparametric modeling of composite materials based on non-intrusive PGD informed by multiscale analyses: Application for real-time stiffness prediction of woven composites*, Composite Structures, **302**, 116228, 2022, https://doi.org/10.1016/j.compstruct.2022.116228.

Received January 28, 2026; revised version July 9, 2026.
Published online September 14, 2026.